PHYSICAL REVIEW B **107**, 224307 (2023)

Light-driven transitions in quantum paraelectrics

Zekun Zhuang,[1,*] Ahana Chakraborty,[1,†] Premala Chandra,[1,‡] Piers Coleman,[1,2,§] and Pavel A. Volkov[1,3,4,∥]
[1]*Center for Materials Theory, Rutgers University, Piscataway, New Jersey 08854, USA*
[2]*Hubbard Theory Consortium, Department of Physics, Royal Holloway, University of London, Egham, Surrey TW20 0EX, United Kingdom*
[3]*Department of Physics, Harvard University, Cambridge, Massachusetts 02138, USA*
[4]*Department of Physics, University of Connecticut, Storrs, Connecticut 06269, USA*

(Received 20 January 2023; revised 22 May 2023; accepted 23 May 2023; published 14 June 2023)

Motivated by recent experiments on pump-induced polar ordering in the quantum paraelectric $\mathrm{SrTiO_3}$, we study a driven phonon system close to a second-order phase transition. Analyzing its classical dynamics, we find that sufficiently strong driving leads to transitions into polar phases whose structures, determined by the light polarization, are not all accessible in equilibrium. In addition, for certain intensity profiles, we demonstrate the possibility of two-step transitions as a function of fluence. For even stronger field intensities, the possibility of period-doubling and chaotic behavior is demonstrated. Finally we develop a generalized formalism that allows us to consider quantum corrections to the classical dynamics in a systematic fashion. We predict a shift in the critical pump fluence due to quantum fluctuations with a characteristic dependence on the fluence increase rate that should be observable in experiment.

DOI: 10.1103/PhysRevB.107.224307

I. INTRODUCTION

The control and design of properties in quantum materials are outstanding goals both to address fundamental questions and to develop applications with quantum advantages. Because the potential and the kinetic energy scales in these materials are comparable, their quantum phases are very sensitive to external fields [1–3]. Advances in the production of strong light pulses in mid-infrared and terahertz ranges [4–6] have led to opportunities for such light to strongly modify the low-energy physics of materials. In particular, light-induced electronic [7,8] and lattice [9–16] phase transitions [17–19] have been observed.

Recently terahertz (THz) field-induced ferroelectricity has been demonstrated in $\mathrm{SrTiO_3}$ (STO) [10,11], in agreement with semiclassical predictions based on nonlinear phonon coupling [20–22]. Though this material remains paraelectric to the lowest temperatures [23], its polar mode can be softened by chemical substitution [24,25] and strain [26] leading to a polar instability. However, unlike these material modifications, the pump-induced phase transition occurs as a function of fluence. Since quantum criticality is observed in $^{18}\mathrm{O}$ doped STO [27–29], there is also the intriguing possibility of driving nonequilibrium quantum critical dynamics in this quantum paraelectric.

For driven classical phase transitions, the creation of topological defects with universal scaling of their density has been predicted and observed in materials [30–32]. Universal dynamics [33–35] have emerged from theoretical studies of dynamical quantum critical effects, as have signatures of dynamical quantum phase transitions such as the Loschmidt echo [36–38]. However these characterizations have predominantly been realized in closed quantum systems like cold atoms where initial states can be carefully prepared [36–38]. By definition, quantum materials are not isolated from their environments and their constituents, unlike those of their synthetic quantum counterparts, cannot be easily addressed microscopically.

The light-induced ferroelectricity experiments [10,11,13,14] thus demand new ways to model strong classical drive protocols that induce critical dynamics, both classical and quantum, and to identify macroscopic signatures of dynamical quantum phase transitions. Theoretical studies suggest that many THz field-induced phenomena may be due to nonlinear phonon interactions [20–22,39–45]. Recently many of the observed features in the field-induced ferroelectricity experiments [10,11] have been simulated [46] with a time-dependent density functional theory analysis where the anharmonic coupling between the driven and the critical phonons is modelled by a Schrödinger-Langevin approach [47]. In parallel a Matsubara action analysis has been developed to describe an off-resonant drive-induced feroelectric transition [48], where results have been obtained using a saddle-point (classical) calculation.

The key idea of light-induced phase transitions is a generalization of optical tweezers [49–51] to many-body physics [1,2]. In the context of optical tweezers, a high-frequency laser mode polarizes the atoms, reducing their energy by an amount proportional to the intensity of the light, producing an effective potential $V_{\mathrm{eff}}(\mathbf{x}) = -\frac{1}{2}\chi_0 E(\mathbf{x})^2$, where χ_0 is the polarizability of the atom. Similarly, in light-induced phase

---

[*] zekun.zhuang@physics.rutgers.edu
[†] ahana@physics.rutgers.edu
[‡] pchandra@physics.rutgers.edu
[§] coleman@physics.rutgers.edu
[∥] pv184@physics.rutgers.edu

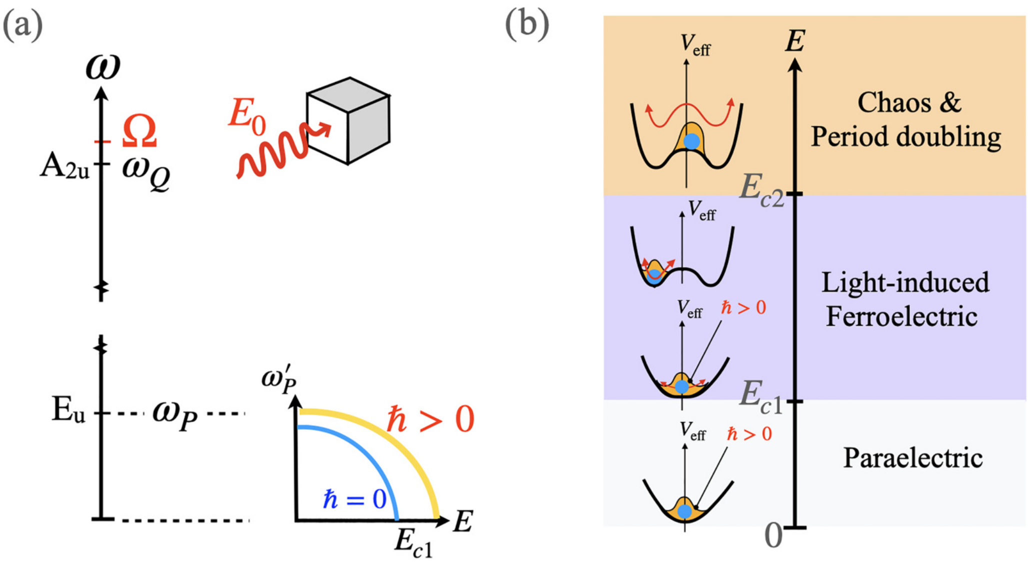

FIG. 1. (a) Schematic of the energy scales in a light-induced experiment, showing the pumping frequency Ω that resonantly drives the high-frequency anharmonic A_{2u} optical mode at frequency ω_Q and the low-frequency soft polar E_u mode. Shown at the bottom is the evolution of the soft polar mode frequency with fluence and the effect of quantum fluctuations ($\hbar > 0$). (b) Phase transitions as a function of electric field amplitude, showing the evolution of an effective potential V_{eff} with increasing fluence. The orange wavepacket around the blue classical configuration represents the effect of quantum fluctuations ($\hbar > 0$).

transitions, the intensity of a high-frequency laser modifies the effective potential of a polar soft mode to be

$$V_{\text{eff}}(P) = \frac{1}{2}(\omega_P^2 - \chi E^2)P^2 + \frac{u}{2}P^4, \tag{1}$$

where P and ω_P are the polarization and frequency of the soft mode respectively, u is the quartic coefficient and χ is the coupling to the electric field intensity E^2. Once the shifted soft mode frequency

$$\omega_P'^2(E) = \omega_P^2 - \chi E^2 \tag{2}$$

vanishes, a phase transition into a broken symmetry state with finite polarization magnitude

$$|P_0| = \sqrt{\frac{-\omega_P'^2(E)}{2u}} \tag{3}$$

occurs. Here we consider a harmonic driving electric field $E(t) = E_0 \cos \Omega t$. Typically, the coupling χ in (1) and (2) is enhanced by resonantly driving an intermediate high-frequency optical phonon that is anharmonically coupled to the polar mode [see Fig. 1(a)]. This process modifies the effective potential of the soft mode, ultimately inducing phase transitions as a function of fluence [see Fig. 1(b)]. More specifically, in addition to the ferroelectric transition, at higher field intensities the polarization fluctuations, $\delta P = |P - P_0|$, become sufficiently large that the system oscillates between the two potential wells ($\delta P \gg |P_0|$) and the system returns to being paraelectric on average. Qualitatively this is because at high fields P_0 grows linearly with E whereas δP increases superlinearly. The latter occurs due to a field-induced hardening of the soft polar mode frequency, that brings it closer to the pump frequency, enhancing the oscillation amplitude. This behavior results in a critical field E_{c2} where $\delta P \approx P_0$ [see Fig. 1(b)].

Since quantum criticality has been observed in a number of quantum paraelectrics at low tempertures [27–29], it is natural to explore how the presence of quantum fluctuations will modify the critical fluence E_{c1} [see Fig. 1(b)] into the polar phase. Qualitatively we expect the renormalized mass $\tilde{m}(t)$, the renormalized quadratic coefficient in the effective potential (1), to have the form

$$\tilde{m}(t) = \omega_P^2 + m_{Cl}(t) + m_Q(t) \tag{4}$$

where the time-dependence of the classical mass corrections, $m_{Cl}(t) = -\chi\{E(t)\}^2$ (cf. (2)), results from the harmonic drive; $m_Q(t)$ refers to the time-dependent quantum mass corrections. Since quantum fluctuations are expected to disorder the system, $m_{Cl}(t)$ and $m_Q(t)$ in (4) act in opposition leading to a shift in the critical point. Nonequlibrium quantum dynamics has been previously studied after a quench to the quantum critical point [33–35], but here a new approach is required to treat dynamical quantum fluctuations when the classical order parameter is finite.

In this paper, we present a theoretical study of light-induced transitions in quantum paraelectrics where we explore their classical dynamics [20–22] with controlled quantum corrections. More specifically, classically we consider the effects of light polarization, long-range Coulomb interactions and drive fluence for the case of a resonantly driven phonon coupled to the soft mode (Sec. II). For a paraelectric with cubic symmetry (Sec. III), we demonstrate fluence- and polarization-dependent transitions into different ordered phases, some inaccessible in equilibrium: for example we find two successive transitions as a function of fluence can occur in contrast to the one-stage symmetry-breaking routinely observed. Finally, we demonstrate (Sec. IV) that the classical dynamical equations [20–22] emerge naturally within a Keldysh field theory. The quantum corrections to these equations can be then be treated systematically in a diagrammatic expansion. We find that the critical fluence to enter the ferroelectric phase E_{c1} [see Fig. 1(b)] is shifted due to quantum fluctuations, a prediction that should be accessible in experiment. Here we have described light-induced transitions as a function of field intensity; an increase in fluence leads to a decrease of $m_{Cl}(t)$ such that $\tilde{m}(t)$ will change sign as a function of time. Thus driven transitions as a function of fluence and of time are closely connected, and this link will be pursued particularly in our study of quantum effects.

II. THE CLASSICAL ACTION WITH CUBIC SYMMETRY

We consider a three-dimensional paraelectric system with cubic symmetry group O_h, where the dipole moment corresponds to the three-fold degenerate irreducible representation t_{1u}. There are a number of cubic quantum paraelectrics including KTaO$_3$, and we note that STO has a weakly distorted tetragonal structure. We assume that the only relevant phonon modes are two sets of t_{1u} optical phonon modes, P_i and Q_i ($i = x, y, z$), where the P and Q are soft polar and higher energy modes, respectively. Consideration of two sets of modes is both motivated by experiment [11], and, as shown below, is necessary to provide a finite lifetime to the transient ferroelectric state after the pump is turned off, consistent with observation [10]. The general classical action for $P_i(x, t)$ and $Q_i(x, t)$ has the form

$$S = S_2 + S_4 + S_C + S_{PQ} + S_E. \tag{5}$$

Here S_2 describes the harmonic terms in the action

$$S_2 = \int_{x,t} \sum_i \frac{1}{2}\big[(\partial_t Q_i)^2 - c_q^2(\nabla Q_i)^2 - \omega_Q^2 Q_i^2 + (\partial_t P_i)^2 - c_p^2(\nabla P_i)^2 - \omega_P^2 P_i^2\big], \tag{6}$$

where $\omega_Q \gg \omega_P$ are the frequencies of the two optical modes, and c_p and c_q are their sound velocities respectively. We will also use the shorthand notation $\int_{x,t} \equiv \int d^3x \int dt$ hereafter. S_4 represents the anharmonic interactions of the modes, taken to be local:

$$S_4 = -\int_{x,t}\left[u_q\left(\sum_i Q_i^2\right)^2 + v_q \sum_i Q_i^4 + u_p\left(\sum_i P_i^2\right)^2 + v_p \sum_i P_i^4\right], \tag{7}$$

where we require $v_{p(q)} > -u_{p(q)}$ if $u_{p(q)} > 0$ and $v_{p(q)} > -3u_{p(q)}$ if $u_{p(q)} < 0$ so that the energy is bounded from below.

The term S_C describes the Coulomb interaction between the charge fluctuations induced by the longitudinal fluctuations of the P and Q modes, which in reciprocal space is given by

$$S_C = -2\pi \int_{k,t} \frac{\rho(k)\rho(-k)}{k^2},$$

$$\rho(k) = i\sum_i Z_P k_i P_i(k) + Z_Q k_i Q_i(k), \tag{8}$$

where $Z_{Q(P)}$ is proportional to the effective charge of the $Q(P)$ mode, and we denote $\int_{k,t} = \int \frac{d^3k}{(2\pi)^3} dt$. This term is responsible for the splitting between the longitudinal and transverse optical modes (LO-TO splitting).

S_{PQ}, the third term in Eq. (5), describes the nonlinear interaction between the P and Q modes. Only coupling between even powers of P and Q leads to qualitatively new effects; by contrast, cubic-linear or linear-linear couplings can be shown to simply renormalize the effects of linear coupling to the electric field (see Appendix A for more discussions). In particular, these terms will lead to contributions $\propto Q(t), Q^3(t), P^2(t)Q(t)$ in the equation of motion for the P mode. Since Q mode is the one being driven by light, these terms will oscillate at the driving frequency (and its multiples) with a zero average. As we show below, such terms are not important for the determination of the onset of the pump-induced ferroelectricity and therefore can be neglected (see also discussion in Sec. III C). Therefore we restrict ourselves to couplings with even powers of P and Q, consistent with cubic symmetry:

$$S_{PQ} = \int_{x,\tau}\left[\frac{\gamma_1}{2}|\vec{P}|^2|\vec{Q}|^2 + \frac{\gamma_2}{2}(\vec{P}\cdot\vec{Q})^2 + \frac{\gamma_3}{2}\sum_i P_i^2 Q_i^2\right].$$

Finally,

$$S_E = \int_{x,t} Z_q \vec{E}\cdot\vec{Q} + Z_p \vec{E}\cdot\vec{P} \tag{9}$$

describes the interaction of a high-frequency external driving field E with the P and Q modes. Importantly, one observes that the light only couples to oscillations of Q or P with antiparallel wave vectors, i.e., $\vec{E}(\vec{k})$ couples to $\vec{Q}(-\vec{k})$ and $\vec{P}(-\vec{k})$, and does not couple to oscillations orthogonal to $\vec{E}$. Since electromagnetic waves are transverse ($\vec{E}\cdot\vec{k} = 0$), the external field couples to transverse modes so that S_C (8) vanishes for the transverse optical modes relevant for our present study due to its longitudinal origin [$\rho(k) \propto \vec{k}\cdot\vec{E}$].

III. CLASSICAL DYNAMICS

In this section, we explore the equations of motion of the P and the Q modes that result from the classical action with cubic symmetry just presented in Sec. II. We discuss the physically reasonable assumptions we make so that these equations can be mapped onto that of a particle moving in an effective potential V_{eff}. The instabilities of V_{eff} are then studied as a function of light polarization (Sec. III A). Intensity profiles associated with second harmonic generation are next presented as experimental signatures of predicted polar phases often not accessible in equilibrium (Sec. III B).

Finally (Sec. III C), we go beyond the effective potential approximation and analyze a minimalist model of two coupled scalar oscillators. The resulting equation of motion is that of a generalized Duffing oscillator and thus is expected to have rich dynamics [52–54]. Indeed, at large fluences, we find parameter regimes where there are multiple steady state solutions and even chaotic behavior. We also find persistence of the polar phase after the drive has ceased, in qualitative agreement with experiment [10,11].

A. Effective potential approximation: Polarization-controlled ferroelectric order

Here we assume the system is homogeneous. Since the typical wavelength of THz/IR light (10^1–10^2 μm) is much larger than the relevant microscopic scales, we restrict our attention to the uniform response of the P and the Q modes. The equations of motion (EOMs) of the Q modes and P modes are then given by

$$\ddot{Q}_i + \omega_Q^2 Q_i + \frac{\partial V_4(Q_i,P_i)}{\partial Q_i} + \frac{\partial V_{PQ}(Q_i,P_i)}{\partial Q_i} + \frac{\partial V_C(Q_i,P_i)}{\partial Q_i} - Z_q E_i = 0, \tag{10}$$

$$\ddot{P}_i + \omega_P^2 P_i + \frac{\partial V_4(Q_i,P_i)}{\partial P_i} + \frac{\partial V_{PQ}(Q_i,P_i)}{\partial P_i} + \frac{\partial V_C(Q_i,P_i)}{\partial P_i} - Z_p E_i = 0, \tag{11}$$

with potentials

$$V_4 = u_q\left(\sum_i Q_i^2\right)^2 + v_q \sum_i Q_i^4 + u_p\left(\sum_i P_i^2\right)^2 + v_p \sum_i P_i^4, \tag{12}$$

$$V_{PQ} = -\frac{\gamma_1}{2}|\vec{P}|^2|\vec{Q}|^2 - \frac{\gamma_2}{2}(\vec{P}\cdot\vec{Q})^2 - \frac{\gamma_3}{2}\sum_i P_i^2 Q_i^2, \tag{13}$$

$$V_C = \sum_{i,j}\left[2\pi Z_p^2 \frac{k_i k_j}{k^2} P_i P_j + 2\pi Z_q^2 \frac{k_i k_j}{k^2} Q_i Q_j + 4\pi Z_p Z_q \frac{k_i k_j}{k^2} Q_i P_j\right], \tag{14}$$

where we implicitly take the long-wavelength limit $\vec{k} \to 0$ and assume a simple harmonic drive $E_i(t) = E_{0,i}\cos\Omega t$. Several approximations are needed to simplify (10) and (11). First, we assume that the high-frequency Q modes are not influenced by any feedback from the low-frequency P modes ($\omega_Q \gg \omega_P$), so that Eq. (10) becomes

$$\ddot{Q}_i + \omega_Q^2 Q_i + 4\pi Z_q^2 \frac{k_i k_j}{k^2} Q_j + 4u_q|\vec{Q}|^2 Q_i + 4v_q Q_i^3 = Z_q E_i, \tag{15}$$

where we have used a summation convention over the repeated subscripts j. Assuming the drive to be weak enough to ignore the cubic terms in Eq. (15), we find that the high-frequency transverse modes are then directly proportional to the driving field,

$$Q_i(t) = \chi_q E_{0,i}\cos\Omega t, \tag{16}$$

where the susceptibility

$$\chi_q = \frac{Z_q}{\omega_Q^2 - \Omega^2}. \tag{17}$$

diverges as $\Omega \to \omega_Q$, reflecting the resonant response of the Q mode to the driving field. Note that the incoming laser beam contains purely transverse fields, so that longitudinal Q modes are not excited [see discussion after Eq. (9)]. This linear approximation reduces Eq. (11) to a decoupled nonlinear differential equation for $\vec{P}$ only.

Next, we assume the solution is rapidly oscillating with frequency $\sim\Omega$ around a time-averaged value $\overline{P_i}$, where $\overline{(\ldots)}$ denotes the time-average over a time interval $\tau \gg 1/\Omega$. The equations for P_i are then obtained by time-averaging Eq. (11) with respect to Qs. The resulting equations are identical to a particle moving in the effective potential:

$$\begin{aligned} V_{\text{eff}} &= \sum_{i,j}\left(\frac{\omega_P^2}{2}\delta_{ij} + 2\pi Z_p^2\frac{k_i k_j}{k^2}\right)P_i P_j + u_p\left(\sum_i P_i^2\right)^2 \\ &\quad + v_p\sum_i P_i^4 - \sum_{i,j}\left[\frac{\gamma_1}{2}\overline{Q_j^2}P_i^2 + \frac{\gamma_2}{2}\overline{Q_iQ_j}P_iP_j + \frac{\gamma_3}{2}\overline{Q_i^2}P_i^2\right] \\ &\equiv \frac{1}{2}\left(\tilde{\omega}_P^2\right)_{ij}P_iP_j + u_P\left(\sum_i P_i^2\right)^2 + v_P\sum_i P_i^4, \end{aligned} \tag{18}$$

where we have employed a summation convention in the final expression. Effective potentials of this sort lie at the heart of light-matter manipulations, and V_{eff} is in essence, a simple extrapolation of the laser-tweezer concept to a many-body phonon potential. We note that using (16), we can rewrite the resonant response of $Q_\alpha = \chi_q E_\alpha$ allowing us to rewrite the effective potential in terms of the driving field

$$\begin{aligned} V_{\text{eff}} &= \sum_{i,j}\left(\frac{\omega_P^2}{2}\delta_{ij} + 2\pi Z_p^2\frac{k_i k_j}{k^2}\right)P_i P_j \\ &\quad + u_p\left(\sum_i P_i^2\right)^2 + v_p\sum_i P_i^4 \\ &\quad - \sum_{i,j}\left[\frac{\tilde{\gamma}_1}{2}\overline{E_j^2}P_i^2 + \frac{\tilde{\gamma}_2}{2}\overline{E_iE_j}P_iP_\beta + \frac{\tilde{\gamma}_3}{2}\overline{E_i^2}P_i^2\right], \end{aligned} \tag{19}$$

where the coefficients $\tilde{\gamma}_i = (\chi_q)^2\gamma_i$ $(i = 1, 2, 3)$ are the resonant response coefficients to the external field. We note that in steady state the time-average $\overline{P_i}$ is expected to lie at the local minimum of V_{eff}.

We now analyze the instabilities resulting from V_{eff} in the presence of a circularly or linearly polarized electromagnetic wave propagating along the z axis, exciting the transverse modes Q_x and Q_y. We assume that the LO-TO splitting $\sim Z_p^2$ is large and only consider the long-wavelength soft transverse phonon modes, for example, $P_{x,y}(0,0,k_z)$ and $P_z(k_x,0,0)$. The excitation of Q modes generates an anisotropic shift in the effective frequency of the soft transverse P phonons. They are defined by the eigenvalues of second derivative matrix of (18), given by

$$\begin{aligned} \left(\tilde{\omega}_P^2\right)_{xx} &= \omega_P^2 - \tilde{\gamma}_1\left(\overline{E_x^2} + \overline{E_y^2}\right) - (\tilde{\gamma}_2 + \tilde{\gamma}_3)\overline{E_x^2}, \\ \left(\tilde{\omega}_P^2\right)_{yy} &= \omega_P^2 - \tilde{\gamma}_1\left(\overline{E_x^2} + \overline{E_y^2}\right) - (\tilde{\gamma}_2 + \tilde{\gamma}_3)\overline{E_y^2}, \\ \left(\tilde{\omega}_P^2\right)_{zz} &= \omega_P^2 - \tilde{\gamma}_1\left(\overline{E_x^2} + \overline{E_y^2}\right), \end{aligned} \tag{20}$$

TABLE I. Nonequilibrium ferroelectric phase evolution under different conditions for light circularly polarized in the x-y plane. The symbol $\{[uvw]\}_n$ denotes the Z_n symmetry breaking phase with polarization along $u\hat{x}+v\hat{y}+w\hat{z}$ or the other $n-1$ equivalent directions related by C_4 rotations about the z axis or reflection in the xy plane ($z \to -z$).

		$2\tilde{\gamma}_1+\tilde{\gamma}_2+\tilde{\gamma}_3>0$		$2\tilde{\gamma}_1+\tilde{\gamma}_2+\tilde{\gamma}_3<0$	
		$\tilde{\gamma}_1>0$	$\tilde{\gamma}_1<0$	$\tilde{\gamma}_1>0$	$\tilde{\gamma}_1<0$
$v_p>0$	$\tilde{\gamma}_2+\tilde{\gamma}_3>0$	$[000]\to\{[110]\}_4$[a] $[000]\to\{[110]\}_4\to\{[aac]\}_8$[b]	$[000]\to\{[110]\}_4$[a] $[000]\to\{[110]\}_4\to\{[aac]\}_8$[b]	$[000]\to\{[001]\}_2$[c] $[000]\to\{[001]\}_2\to\{[aac]\}_8$[d]	[000]
	$\tilde{\gamma}_2+\tilde{\gamma}_3<0$	$[000]\to\{[001]\}_2\to\{[aac]\}_8$	$[000]\to\{[110]\}_4$[a] $[000]\to\{[110]\}_4\to\{[aac]\}_8$[b]	$[000]\to\{[001]\}_2$[c] $[000]\to\{[001]\}_2\to\{[aac]\}_8$[d]	[000]
$v_p<0$	$\tilde{\gamma}_2+\tilde{\gamma}_3>0$	$[000]\to\{[100]\}_4$	$[000]\to\{[100]\}_4$	$[000]\to\{[001]\}_2$[c] $[000]\to\{[001]\}_2\to\{[aac]\}_8$[d]	[000]
	$\tilde{\gamma}_2+\tilde{\gamma}_3<0$	$[000]\to\{[001]\}_2$	$[000]\to\{[100]\}_4$	$[000]\to\{[001]\}_2$[c] $[000]\to\{[001]\}_2\to\{[aac]\}_8$[d]	[000]

[a]If $\frac{2u_p}{2u_p+v_p}\in\left(\frac{2\tilde{\gamma}_1}{2\tilde{\gamma}_1+\tilde{\gamma}_2+\tilde{\gamma}_3},+\infty\right)$; [b]If $\frac{2u_p}{2u_p+v_p}\in\left(-\infty,\frac{2\tilde{\gamma}_1}{2\tilde{\gamma}_1+\tilde{\gamma}_2+\tilde{\gamma}_3}\right)$; [c]If $\frac{u_p+v_p}{u_p}\notin\left(\frac{2\tilde{\gamma}_1}{2\tilde{\gamma}_1+\tilde{\gamma}_2+\tilde{\gamma}_3},0\right)$; [d]If $\frac{u_p+v_p}{u_p}\in\left(\frac{2\tilde{\gamma}_1}{2\tilde{\gamma}_1+\tilde{\gamma}_2+\tilde{\gamma}_3},0\right)$.

Note that we have used $\overline{E_xE_y}=0$. For circularly polarized light running along the z axis $\overline{E_x^2}=\overline{E_y^2}=\frac{1}{2}E_{0,x}^2=\frac{1}{2}E_{0,y}^2$, and then Eq. (20) becomes

$$\left(\tilde{\omega}_P^2\right)_{xx}=\left(\tilde{\omega}_P^2\right)_{yy}=\omega_P^2-(2\tilde{\gamma}_1+\tilde{\gamma}_2+\tilde{\gamma}_3)\overline{E_x^2},$$
$$\left(\tilde{\omega}_P^2\right)_{zz}=\omega_P^2-2\tilde{\gamma}_1\overline{E_x^2}. \tag{21}$$

Suppose that both $\tilde{\gamma}_1>0$ and $2\tilde{\gamma}_1+\tilde{\gamma}_2+\tilde{\gamma}_3>0$ are positive. If $\tilde{\gamma}_2+\tilde{\gamma}_3>0$, then as the magnitude of drive increases, the transverse mode frequencies $(\tilde{\omega}_P^2)_{xx}=(\tilde{\omega}_P^2)_{yy}$ vanish first, giving rise to a spontaneous polarization in the x-y plane in the steady state once $\overline{E_{x(y)}^2}>\omega_p^2/(2\tilde{\gamma}_1+\tilde{\gamma}_2+\tilde{\gamma}_3)$. The direction of the polarization that develops is determined by the anisotropy constant v_p. From Eq. (18), one finds that the effective potential $V_{\rm eff}$ is minimized by $\vec{P}$ along [±110] if $v_p>0$ and by $\vec{P}$ along [100] or [010] if $v_p<0$.

Let us now consider enhancing the drive fluence beyond the critical one. Note that Eq. (21) no longer determines the phonon frequencies, and the stability of the system is determined by the Hessian matrix at the new energy minimum with nonzero $\vec{P}$. Let us focus on the case $v_p>0$. If the drive $\overline{E_{x(y)}^2}$ is increased beyond the first instability threshold, the frequency for the transverse P_z mode around the new minimum will soften at a second critical fluence, if the parameters obey certain constraints (see Table I). This gives rise to a second phase transition. For light with linear polarization along the x axis, the effective frequency Eq. (20) can be similarly determined by setting $\overline{E_y^2}=0$.

Tables I and II summarize various possible ferroelectric orderings that are possible in the effective potential approximation with circular (Table I) and linear (Table II) light polarizations. There are multiple continuous phase transitions when $\overline{E^2}$ (proportional to the intensity of light), varies. Importantly, in equilibrium only $[111]_8$ (for $v_P>0$) or $[100]_6$ (for $v_P<0$, sixfold degenerate due to cubic symmetry) phases can be realized by tuning ω_P^2. Therefore our analysis shows that an external drive can induce ferroelectric phases that are inaccessible in equilibrium. In Fig. 2, we show illustrative examples of two-stage symmetry-breaking driven by circularly and linearly polarized light that do not occur in thermal polar pathways.

B. Second harmonic generation signatures

Experimentally, nonequilibrium ferroelectricity is detected via second harmonic generation (SHG) [10,11]. Due to the nonlinearity, a monochromatic electric field with frequency ω induces dipole moments oscillating at a doubled frequency 2ω, described by the second-order nonlinear optical susceptibility tensor χ [55]

$$P_i(2\omega)=\chi_{ijk}E_j(\omega)E_k(\omega). \tag{22}$$

The dipole moments then act as a source and generate a second harmonic of frequency 2ω and intensity $I_i(2\omega)\propto|P_i(2\omega)|^2$.

For centrosymmetric systems, the absence of inversion symmetry breaking causes all elements of χ vanish, so there is no SHG. For noncentrosymmetric systems, the residual symmetry typically reduces the eighteen independent tensor elements to only a few, constraining the relation of intensities along different directions. For example, consider the $\{[110]\}_4$ phase listed in Table I, described by the effective potential

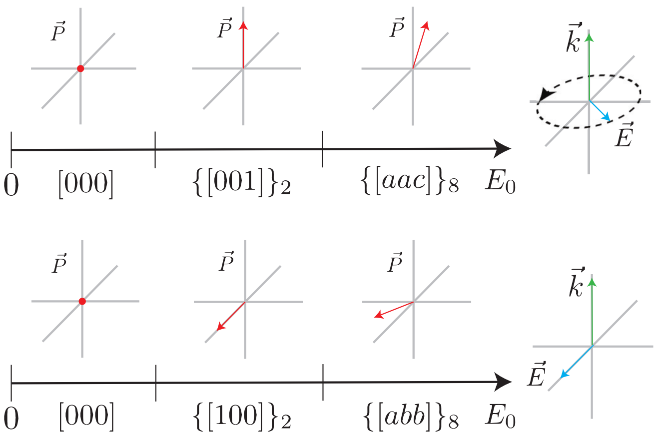

FIG. 2. Schematics of two illustrative examples for the nonthermal pathways considered: multiple polar phase transitions as a function of electric field amplitude in cubic paraelectric systems. (Top) Light is circularly polarized in the x-y plane with $v_p>0$, $\tilde{\gamma}_1>0$, $\tilde{\gamma}_2+\tilde{\gamma}_3<0$, and $2\tilde{\gamma}_1+\tilde{\gamma}_2+\tilde{\gamma}_3>0$. (Bottom) Light is linearly polarized along the x axis with $v_p>0$, $\tilde{\gamma}_1>0$, $\tilde{\gamma}_2+\tilde{\gamma}_3>0$, and $\tilde{\gamma}_1+\tilde{\gamma}_2+\tilde{\gamma}_3>0$.

TABLE II. Nonequilibrium ferroelectric phase evolution under different conditions when light is linearly polarized in the x direction. The notation is same as that in Table I except that different Z_n symmetry breaking phases are related by C_4 rotation around x axis and reflection with respect to the yz plane ($x \to -x$).

		$\tilde{\gamma}_1 > 0$		$\tilde{\gamma}_1 < 0$	
		$\tilde{\gamma}_1 + \tilde{\gamma}_2 + \tilde{\gamma}_3 > 0$	$\tilde{\gamma}_1 + \tilde{\gamma}_2 + \tilde{\gamma}_3 < 0$	$\tilde{\gamma}_1 + \tilde{\gamma}_2 + \tilde{\gamma}_3 > 0$	$\tilde{\gamma}_1 + \tilde{\gamma}_2 + \tilde{\gamma}_3 < 0$
$v_p > 0$	$\tilde{\gamma}_2 + \tilde{\gamma}_3 < 0$	$[000] \to \{[011]\}_4$[a] $[000] \to \{[011]\}_4 \to \{[abb]\}_8$[b]	$[000] \to \{[011]\}_4$[a] $[000] \to \{[011]\}_4 \to \{[abb]\}_8$[b]	$[000] \to \{[100]\}_2$[c] $[000] \to \{[100]\}_2 \to \{[abb]\}_8$[d]	[000]
	$\tilde{\gamma}_2 + \tilde{\gamma}_3 > 0$	$[000] \to \{[100]\}_2 \to \{[abb]\}_8$	$[000] \to \{[011]\}_4$[a] $[000] \to \{[011]\}_4 \to \{[abb]\}_8$[b]	$[000] \to \{[100]\}_2$[c] $[000] \to \{[100]\}_2 \to \{[abb]\}_8$[d]	[000]
$v_p < 0$	$\tilde{\gamma}_2 + \tilde{\gamma}_3 < 0$	$[000] \to \{[010]\}_4$	$[000] \to \{[010]\}_4$	$[000] \to \{[100]\}_2$[c] $[000] \to \{[100]\}_2 \to \{[abb]\}_8$[d]	[000]
	$\tilde{\gamma}_2 + \tilde{\gamma}_3 > 0$	$[000] \to \{[100]\}_2$	$[000] \to \{[010]\}_4$	$[000] \to \{[100]\}_2$[c] $[000] \to \{[100]\}_2 \to \{[abb]\}_8$[d]	[000]

[a]If $\frac{2u_p}{2u_p+v_p} \in \left(\frac{\tilde{\gamma}_1+\tilde{\gamma}_2+\tilde{\gamma}_3}{\tilde{\gamma}_1}, +\infty\right)$; [b]If $\frac{2u_p}{2u_p+v_p} \in \left(-\infty, \frac{\tilde{\gamma}_1+\tilde{\gamma}_2+\tilde{\gamma}_3}{\tilde{\gamma}_1}\right)$; [c]If $\frac{u_p+v_p}{u_p} \notin \left(\frac{\tilde{\gamma}_1+\tilde{\gamma}_2+\tilde{\gamma}_3}{\tilde{\gamma}_1}, 0\right)$; [d]If $\frac{u_p+v_p}{u_p} \in \left(\frac{\tilde{\gamma}_1+\tilde{\gamma}_2+\tilde{\gamma}_3}{\tilde{\gamma}_1}, 0\right)$.

Eqs. (18) and (21). The polarized incident light breaks the symmetry between x, y and z directions, so the ferroelectric phase with $\vec{P} = (P_0, \pm P_0, 0)$ only has C_{2v} symmetry along the $\hat{n} = [1, \pm 1, 0]$ axis. For convenience, we denote the symmetry axis $\hat{n}$ as z' and the other two perpendicular directions as x' and y', referred as the crystal frame. For C_{2v} symmetry, there are only five nonzero independent tensor elements, that is $\chi'_{xzx} = \chi'_{xxz}, \chi'_{yyz} = \chi'_{yzy}, \chi'_{zxx}, \chi'_{zyy}, \chi'_{zzz}$ in the crystal frame. Suppose that the material interacts with a probe pulse with linear polarization along $\hat{\theta}' = \cos\theta \hat{z}' + \sin\theta \hat{x}'$ direction, using Eq. (22), one obtains

$$\begin{aligned} P'_z &= E^2(\chi'_{zxx} \sin^2\theta + \chi'_{zzz} \cos^2\theta), \\ P'_x &= E^2 \chi'_{xzx} \sin 2\theta, \\ P'_y &= 0 \end{aligned} \tag{23}$$

in the crystal frame. Consider $\{[aac]\}_8$ in Table I as another example. It has C_{1h} symmetry and the mirror plane is perpendicular to $\hat{y}'$. Besides the five nonzero elements in C_{2v}, there are other five nonvanishing elements: $\chi'_{xxx}, \chi'_{xyy}, \chi'_{xzz}, \chi'_{yxy} = \chi'_{yyx}, \chi'_{zzx} = \chi'_{zxz}$. Thus for probe pulse with polarization along $\hat{\theta}'$, one has

$$\begin{aligned} P'_z &= E^2(\chi'_{zxx} \sin^2\theta + \chi'_{zzz} \cos^2\theta + \chi'_{xzx} \sin 2\theta), \\ P'_x &= E^2(\chi'_{xxx} \sin^2\theta + \chi'_{xzz} \cos^2\theta + \chi'_{xzx} \sin 2\theta), \\ P'_y &= 0. \end{aligned} \tag{24}$$

Thus one can observe a change of profile $P_i(\theta)$ when there is nonequilibrium phase transition. In Fig. 3, we show the typical profile of $P_i(\theta)$ for some of the high-symmetry phases, which is experimentally measurable [11].

C. Minimalist coupled oscillator model

We now go beyond the effective potential approximation to study the dynamics of anharmonically coupled oscillators. For simplicity, we consider a minimalist model with two scalar harmonic oscillators P and Q. The real-time action is given by

$$S = \int dt \left[\frac{1}{2}\dot{Q}^2 - \frac{1}{2}\omega_Q^2 Q^2 + \frac{1}{2}\dot{P}^2 - \frac{1}{2}\omega_P^2 P^2 - \frac{1}{4}\alpha P^4 + \frac{\gamma}{2} P^2 Q^2 + Z_q Q E + Z_p P E \right], \tag{25}$$

where $\alpha > 0$ and we assume $\omega_Q \ll \omega_P \approx \Omega$. To obtain this model, we have restricted ourselves to the uniform states and neglected insignificant terms to our interests, such as the anharmonic interactions of Q modes. We also neglected linear-linear and linear-cubic couplings between P and Q modes. These couplings lead to terms in the equation of motion oscillating with frequency Ω and its multiples with zero average, therefore we suggest that their effects should be qualitatively similar to the effect of direct coupling Z_p to the oscillating electric field (see Appendix A for more discussions and numerical justification). In particular, the effect of the linear P-Q coupling can be absorbed into the renormalization of the coupling of P mode to light Z_p. We leave the detailed study of possible additional effects of cubic-linear couplings (such as higher harmonic driving effects) to future work. Note that we are working in the regime where the Q mode is only driven quasiresonantly where the amplitude of Q mode is not too large and the nonlinearity of Q mode, whose effect has been studied in Ref. [22], does not play an important role. This simplified model could describe the nonequilibrium PE-FE transition driven by the external electric field, given that the unstable soft phonon mode is nondegenerate near the phase transition, which is true for Z_2 symmetry breaking transitions listed in Tables I and II.

The classical equations of motion (EOMs) resulting from Eq. (25) are

$$\ddot{Q} + \omega_Q^2 Q + \beta_1 \dot{Q} - \gamma P^2 Q = Z_q E(t), \tag{26}$$

$$\ddot{P} + \omega_P^2 P + \beta_0 \dot{P} - \gamma Q^2 P + \alpha P^3 = Z_p E(t), \tag{27}$$

where we have added extra phenomenological damping terms $\beta_1 \dot{Q}$ and $\beta_0 \dot{P}$. Since the P mode is driven off-resonantly by the E field, we expect the magnitude of P to be small so that $\gamma \overline{P^2} \ll \omega_Q^2$, and we may ignore the nonlinear term in Eq. (26). Neglecting damping, we obtain the steady state solution

$$Q(t) = \chi_q E_0 \cos(\Omega t), \tag{28}$$

where

$$\chi_q = Z_q / (\omega_Q^2 - \Omega^2) \tag{29}$$

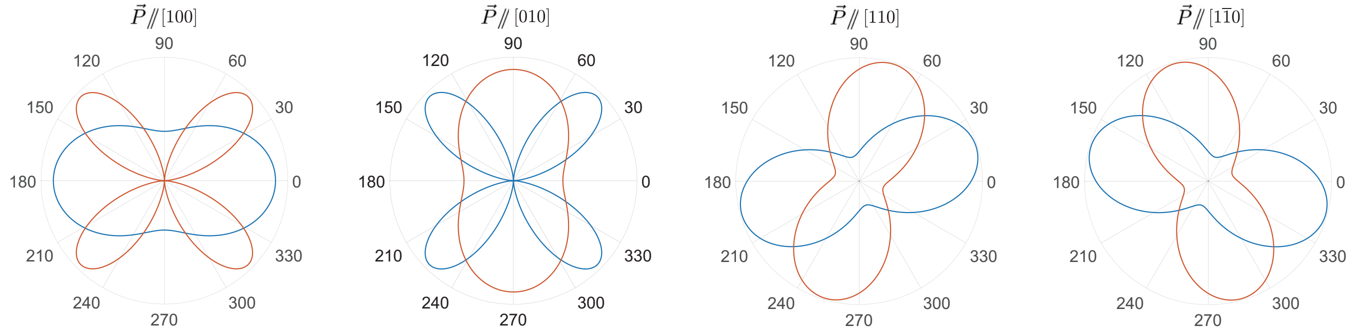

FIG. 3. Typical angular dependence of intensity $I_x(\theta)$ (blue) and $I_y(\theta)$ (red) of second harmonic light in laboratory frame for some of the nonequilibrium ferroelectric phases with high symmetry. The linearly-polarized probe pulse propagates along z direction and the angle between light polarization and x axis is θ. For phases with C_{2v} symmetry, we choose the nonlinear susceptibility in the crystal frame to be $\chi'_{zxx} = 1$, $\chi'_{zzz} = 1.5$, and $\chi'_{xzx} = 0.4$. Note that we have rescaled some of the curves to make their magnitudes comparable.

is the resonant Q susceptibility introduced in (17) and Eq. (27) becomes

$$\ddot{P} + \left(\omega_P^2 + m(t)\right)P + \alpha P^3 = Z_p E(t), \tag{30}$$

where $m(t) = -\gamma Q^2(t)$ is the time-dependent mass arising from the P^2Q^2 interaction. For convenience, we write the above equation as

$$\ddot{P} + \left(\omega_P^2 - \gamma\overline{Q^2}\right)P + \alpha P^3 = Z_p E(t) + f(t), \tag{31}$$

where $\overline{Q^2} = \frac{1}{2}(\chi_q E_0)^2$ is the time-average of the rapidly oscillating Q mode and $f(t) = \frac{1}{2}\gamma\chi_q^2(E_0)^2\cos(2\Omega t)P$. When $\omega_P^2 - \gamma\overline{Q^2} > 0$, the eigenfrequency of the P oscillator remains positive so one expects that P mode oscillates around the global minimum $P = 0$. However when $\omega_P^2 - \gamma\overline{Q^2} < 0$, the mass of the P mode becomes negative and the system becomes ferroelectric in the absence of time-dependent terms, with finite polarization $P_0 = \pm\sqrt{\omega_P'^2/2\alpha}$ as shown in Fig. 4(a). Here

$$(\omega'_P)^2 = 2\left(\gamma\overline{Q^2} - \omega_P^2\right) = 2\left(\tilde{\gamma}\overline{E^2} - \omega_P^2\right), \tag{32}$$

is the eigenfrequency for oscillations in the ferro-electric state and $\tilde{\gamma} = \gamma\chi_q^2$ is the isotropic version of the resonant response coefficients introduced in (19). In the presence of $E(t)$ and $f(t)$, P periodically oscillates around P_0 in the steady state, as seen in Figs. 4(b) and 4(e). We may expand the potential around P_0, approximate P in $f(t)$ by P_0 in Eq. (31) to obtain the steady state solution

$$\delta P(t) \approx \frac{Z_p E_0}{\omega_P'^2 - \Omega^2}\cos(\Omega t) + \frac{\omega_P'^2 + 2\omega_P^2}{2\left(\omega_P'^2 - 4\Omega^2\right)}P_0\cos(2\Omega t), \tag{33}$$

where $\delta P(t) = P - P_0$. This approximation works well when the maximum oscillation amplitude δP_e is much smaller than the time-averaged polarization $\overline{P} \approx P_0$, $\delta P_e/|P_0| \ll 1$. The term $\delta f(t) \propto \cos(2\Omega t)\delta P$ that we have neglected reduces $|\overline{P}|$, which can be seen by substituting Eq. (33) into $\delta f(t)$ and averaging over time. The discrepancies between the exact numerical solutions and the approximate solution Eq. (33) displayed in Fig. 4(a) become substantial once $\delta P/|P_0| \sim O(1)$.

In order for the system to exhibit a macroscopic polarization, the oscillations in the polarization must not exceed the width of the potential well, i.e., the magnitude of oscillation δP_e (33) must be smaller than $|P_0|$, or

$$\frac{Z_p E_0}{\Omega^2 - \omega_P'^2} + \frac{\omega_P'^2 + 2\omega_P^2}{2\left(4\Omega^2 - \omega_P'^2\right)}\sqrt{\frac{\omega_P'^2}{2\alpha}} \lesssim \sqrt{\frac{\omega_P'^2}{2\alpha}}. \tag{34}$$

Note that as the two contributions in Eq. (33) are phase coherent and in phase, the total magnitude is simply the sum of its separate parts. For $Z_p = 0$ and $\omega_P, \omega'_P \ll \Omega$, we observe that the inequality is always fulfilled, i.e., the system becomes ferroelectric for infinitesimal ω'_P. If $Z_p \neq 0$, we can neglect the second term in Eq. (34) for sufficiently low ω'_P. The critical fields E_c can then be estimated by solving

$$\delta P_e \equiv \frac{Z_p E_c}{\Omega^2 - \omega_P'^2} = \sqrt{\frac{\omega_P'^2}{2\alpha}} \equiv |P_0|. \tag{35}$$

Using (32) to express $\omega_P'^2 = 2\tilde{\gamma}(E_c^2 - E_{c0}^2)$, where $E_{c0}^2 = \omega_P^2/\tilde{\gamma}$, we can cast this equation in the dimensionless form

$$\left(\frac{E_Z^2}{E_{c0}^2}\right)x = (x-1)(x-(r^2+1))^2, \tag{36}$$

where $x = (E_c/E_{c0})^2$ $(1 \leqslant x \leqslant r^2+1)$, $E_Z^2 = \frac{Z_p^2\alpha}{2\tilde{\gamma}^2\omega_P^2}$ and $r^2 = \frac{\Omega^2}{2\omega_P^2}$. In the limit of small Z_p, this gives the limiting values $x = 1$ corresponding to the lower critical field $\lim_{Z_p\to 0} E_{c1} = E_{c0}$ and $x = 1 + r^2$, corresponding to the higher critical field

$$\lim_{Z_p\to 0} E_{c2} = E_{c0}\sqrt{1 + \frac{1}{2}\left(\frac{\Omega^2}{\omega_P^2}\right)}. \tag{37}$$

Figure 5 shows the dependence of $|P_0|$ and δP_e on the electric field strength E_0. Note that δP_e first grows linearly with E_0, and then increases superlinearly as the denominator $\Omega^2 - \omega_P'^2$ decreases due to the hardening of phonon frequency ω'_P. By contrast, $|P_0|$ increases linearly at large E_0. Therefore, for $Z_p \lesssim Z_q\frac{\Omega^2}{|\omega_Q^2 - \Omega^2|}\sqrt{\frac{\gamma}{2\alpha}}$, Eq. (35) has two solutions as shown in Fig. 5, which correspond to the estimated lower and higher critical fields. The ferroelectric phase with nonzero steady-state polarization therefore exists only between these two field values.

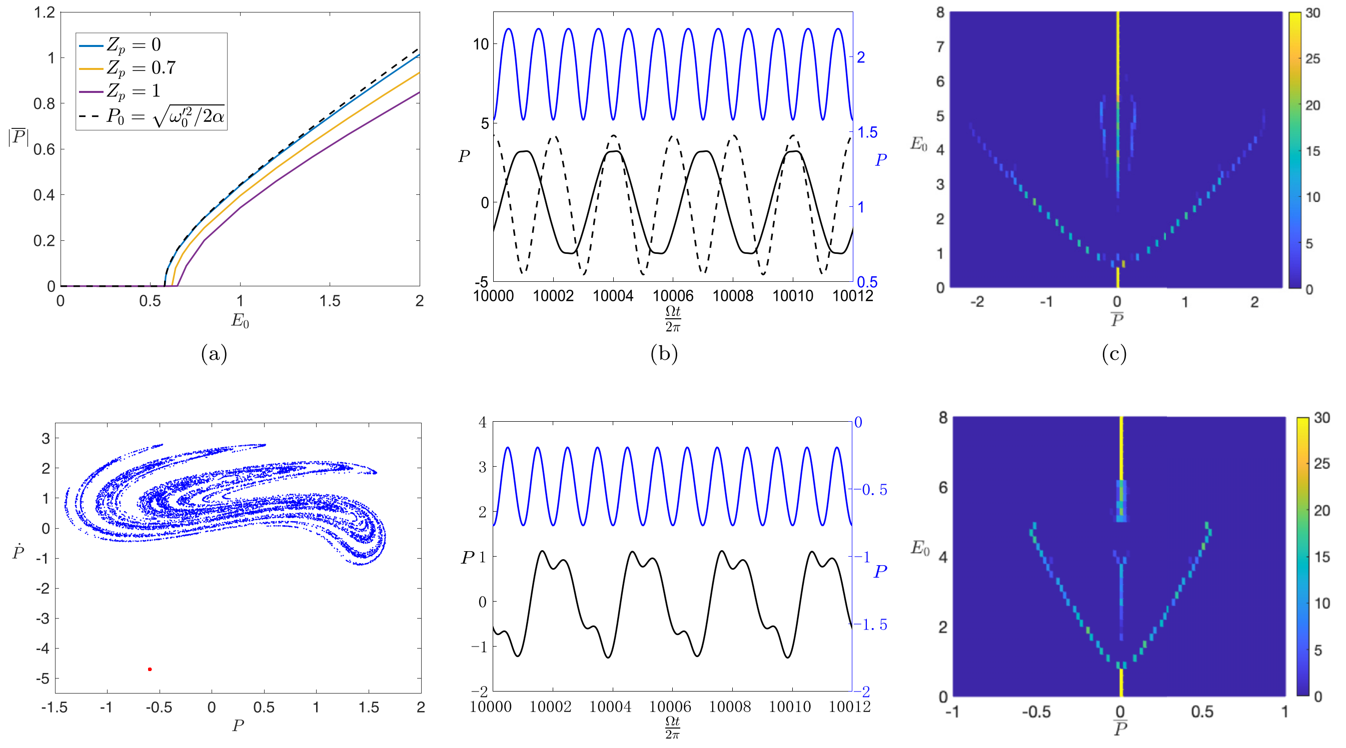

(a) (b) (c)

(d) (e) (f)

FIG. 4. (a) Time-averaged polarization $\overline{P}$ versus electric field strength E_0. The solid lines are the numerical solutions of Eq. (25) for different Z_p, while the dashed line is the analytic solution $P_0 = \pm\sqrt{\omega_P'^2/2\alpha}$ when time-dependent terms is absent. [(b) and (e)] Polarization versus time in the steady state when $E_0 = 4, Z_p = 0.3$, obtained by numerical method; the blue line is the regular solution approximately captured by Eq. (33) while the black lines correspond to the solutions with frequency fractional of Ω. [(c) and (f)] Possible values of $\overline{P}$ vs E_0 when $Z_p = 0.3$; the result is obtained with 30 random initial conditions for each fixed E_0, and the color of grids indicates the number of times the system reaches $\overline{P}$ in its steady state. (d) The Poincaré section when $E_0 = 5.1, Z_p = 0.3$, suggesting the coexistence of chaotic behavior (blue) and periodic solution (red), i.e., KAM structure [56]. All the steady state solution is obtained by numerically solving Eqs. (26) and (27). Common parameter values for all plots: $\omega_P = 0.1, \omega_Q = 2, \Omega = 2.1, \gamma = 0.01, Z_q = 1$, For (a)–(c), we choose $\alpha = 0.1, \beta_1 = \beta_0 = 0.002$; for (d) and (e), we choose $\alpha = 1, \beta_1 = \beta_0 = 0.1$.

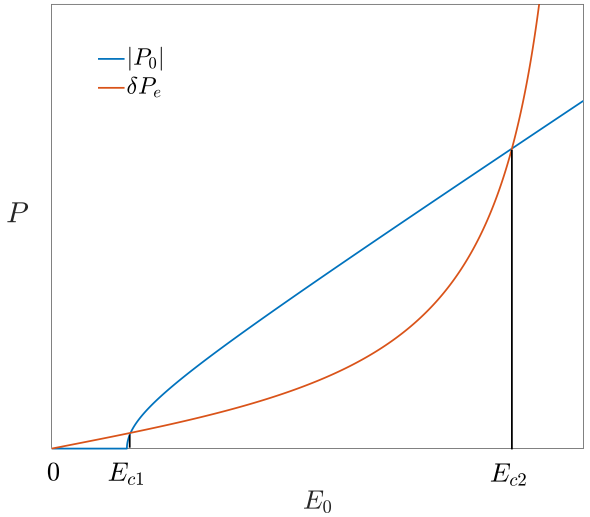

FIG. 5. Field dependence of the steady-state polarization $|P_0|$ and the amplitude of rapid oscillations δP_e [see (35)]. For $\delta P_e > |P_0|$, the rapid oscillations can no longer be neglected, having the effect of reducing the observable steady-state polarization to zero.

For $\omega_p' \ll \Omega$, the system first becomes ferroelectric when $\omega_P' \approx \sqrt{2\alpha}Z_pE_0/\Omega^2$, resulting in shifted critical values E_{c1}, consistent with the numerical results in Fig. 4(a). For sufficiently large $E_0 \gtrsim E_{c2}$, the P oscillator hops between the two minima as $\delta P_e \gtrsim |P_0|$, leading to a reentrant paraelectric phase. Re-entrant para-electricity has been observed in previous numerical simulations [20,21]. Indeed, as seen from Figs. 4(c) and 4(f), the regular solutions described by Eq. (33) finally disappear at sufficiently large E_0.

Remarkably, at intermediate E_0 we also observe other solutions with negligible $\overline{P}$, coexisting with the regular solutions. From Figs. 4(b). and 4(e), one can see that these multiple solutions may have frequency fractional of Ω. We also find chaotic behavior in certain parameter range. Particularly, choosing different initial conditions, we find two different orbits near the onset of chaos [see Fig. 4(d)]. This suggests the coexistence of chaotic behavior with the periodic solution, known as the Kolmogorov-Arnold-Moser (KAM) structure [56]. Indeed we note that Eq. (31) is the equation of motion of a Duffing oscillator, generalized due to the additional $f(t)$ term, that is known to exhibit period-doubling bifurcation and chaotic behavior in certain parameter regimes [52–54].

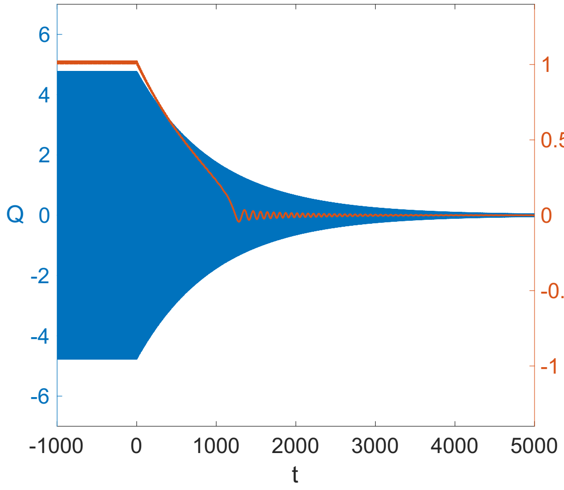

FIG. 6. Polarization vs time after the electric field is turned off at $t = 0$. We choose $Z_p = 0$ and $E_0 = 2$ when the electric field is on, and set $\beta_1 = \beta_0 = 0.002$ all the time. The rest of parameters are the same as that in Fig. 4.

It is useful to have an estimate for the critical electric field strength when finite polarization appears and vanishes. We assume $\omega_Q^2 = 1136.1$ meV Å^{-2} amu^{-1}, $\omega_P^2 = 1.39$ meV Å^{-2} amu^{-1}, $\alpha = 206.9$ meV Å^{-4} amu^{-2}, $\gamma = 11.6$ meV Å^{-4} amu^{-2}, and $Z_p \approx Z_q = 1.15\, e$ amu$^{-1/2}$, which are consistent with the parameters for strained KTaO$_3$ [21]. The double well forms when $|Q_c| \sim 0.346$ Å amu$^{1/2}$, which corresponds to the electric field $E_{c0} \sim 2.7$ MV/cm if one neglects dissipation and takes $\Omega^2 = 1200$ meV Å^{-2} amu^{-1}. Enforcing condition Eq. (34) one obtains a rough estimate of the lower critical electric field $E_{c1} \approx 2.9$ MV/cm and the higher critical electric field $E_{c2} \approx 45.6$ MV/cm (which compares with the more approximate estimate (37), which gives $E_{c2} \sim 60$ MV/cm). Note that E_{c2} corresponds to a large amplitude oscillation $|Q| \sim 5.8$ Å amu$^{1/2}$, suggesting the necessity to include nonlinearity of the Q mode. For example, if quartic terms of Q mode are included, such large oscillation amplitudes are suppressed and it may be possible to observe the vanishing of polarization at a higher critical field E_{c2}. We note that our predicted electric field strengths are approachable in experiments where light pulses with large peak fields (estimated around 18 MV/cm [11]) are used.

In experiments, the driving is not continuous but is rather performed with finite pulses [10,11] and the nonequilibrium polarization persists after the pump has been turned off. In our model, after the external field is turned off, the excited P and Q mode relax due to dissipation resulting in the decay of polarization. As shown in Fig. 6, after the electric field is off, the amplitude of the P mode decays but remains finite, until it eventually oscillates around its equilibrium position. This can be understood by noticing that the effective potential felt by P mode gradually relaxes to its equilibrium form due to the damped motion of Q. The P mode oscillates around the instantaneous minimum of the effective potential, which becomes zero once Q^2 becomes smaller then the critical value for the steady-state driven ferroelectricity. Therefore the system keeps its "memory" of the pump-induced order for times of order of the Q mode lifetime. This qualitatively describes the observed persistence of the polarization after the pump is removed [10,11], though persistence timescales have been reported that are longer than what is accessible in our approach [11].

IV. QUANTUM EFFECTS IN THE PHASE TRANSITION

We now move to a consideration of quantum effects in light-driven ferroelectricity. Previous approaches [33–35] focused on quenches close to a QCP.

Here we develop a formalism appropriate to our situation where quantum fluctuations coexist with significant classical ones. In Sec. IV A, we demonstrate how the classical equations of motion, Eq. (30), arise from a quantum Keldysh action for the case of a single nonlinear oscillator and study the quantum corrections in Sec. IV C, where generalizations to include the momentum dispersion of phonons are discussed. The shift of the critical point due to quantum mass corrections is determined as a function of pumping rate, and this should be accessible in experiment.

We start with the reduced model for a soft phonon mode $P(t)$ described in Eq. (30), with effective Lagrangian

$$\mathcal{L}[P] = \frac{\dot{P}^2}{2} - \left(\omega_P^2 + m(t)\right)\frac{P^2}{2} - \frac{\alpha}{4}P^4 + PE(t). \tag{38}$$

The time-dependent $m(t)$ describes the effect of driving on the P modes: we recall that the drive excites the fast Q modes which, within a classical description, modifies the mass of the slow P mode via biquadratic interactions. The P mode is also linearly coupled to the (classical) electric field, $E(t)$; for the purpose of discussion, we have set the effective charge in (30) to one, $Z_p = 1$.

We now quantize this description, describing how we can formulate a path-integral diagramatic approach. The quantum Hamiltonian is

$$\hat{H} = \frac{\hat{\pi}^2}{2} + \left(\omega_P^2 + m(t)\right)\frac{\hat{P}^2}{2} + \frac{\alpha}{4}\hat{P}^4 - \hat{P}E(t), \tag{39}$$

where $\hat{\pi}$ is the canonical momentum, satisfying $[\hat{P}, \hat{\pi}] = i\hbar$. We now adopt a Schwinger-Keldysh approach considering a time-evolution from a state of thermal equilibrium in the distant past. The generating function $Z_K[E]$ is written as a time-ordered exponential of the Hamiltonian over the Keldysh contour in time, $\{\mathcal{C} : t \in -\infty \longrightarrow \infty \longrightarrow -\infty\}$ running from the past out to the future and back,

$$Z_K[E] = \mathrm{Tr}[\hat{\rho}_0 \mathcal{U}_C], \tag{40}$$

where $\hat{\rho}_0 = e^{-\beta \hat{H}_0}$ is the initial thermal density matrix (we will take $T = 0$ in our final results), while

$$U_C = U_{-\infty,\infty}U_{\infty,-\infty} = T_C e^{-\frac{i}{\hbar}\int_C dt H(t)}, \tag{41}$$

where T_C denotes path-ordering along the contour $\mathcal{C}$. $Z_K[E]$ is recast as a path integral,

$$Z_K[E] = \int_C D[P] e^{i S_K/\hbar}. \tag{42}$$

The action $\mathcal{S}_K$ divides into contributions from the outward and return paths,

$$\mathcal{S}_K = \int_{\mathcal{C}} dt \mathcal{L}[P] = \int_{-\infty}^{\infty} dt[\mathcal{L}[P_+] - \mathcal{L}[P_-]], \tag{43}$$

where $P_+(t)$ and $P_-(t)$ are the integration variables on the outward and return paths, respectively [57]. Under the physical Heisenberg equations of motion, there is strictly one quantum operator $\hat{P}(t)$ and source term $E(t)$ at each point in time, but the Keldysh path integral explores the paths on the upper and lower contours independently, and a complete generating function must consider independent sources $E_\pm(t)$ on the outward and return contours, setting $E_\pm(t) = E(t)$ to recover the physical expectation values.

Variations of the generating function $Z_K(E)$ with respect to the source field E generate correlation functions of the quantum operators $\hat{P}(t)$, path-ordered along the Keldysh contour [58], such that

$$-i\hbar \frac{\delta}{\delta E(t)} \longrightarrow \hat{P}(t). \tag{44}$$

For instance,

$$\begin{aligned} \frac{(-i\hbar)^2}{Z} \frac{\delta^2 Z}{\delta E(t_2)\delta E(t_1)} &\to \frac{1}{Z}\int \mathcal{D}[P]P(t_1)P(t_2)e^{i\mathcal{S}_K/\hbar} \\ &= \langle T_C \hat{P}(t_1)\hat{P}(t_2)\rangle. \end{aligned} \tag{45}$$

We adopt a classical-quantum basis

$$\begin{aligned} P_{cl}(t) &= (P_+ + P_-)/2, \\ P_q(t) &= (P_+ - P_-), \end{aligned} \tag{46}$$

where the classical and quantum variables, P_{cl} and P_q, respectively, are analagous to the the center of mass, and relative coordinates of two body dynamics. Note that our notation differs from Refs. [57,59] by a factor of two in P_q, which simplifies some of the intermediate calculations, but without affecting the final results. The connectivity of the forward and backward paths causes the joint Green's function $\langle P_q(t)P_q(t')\rangle = 0$ to vanish, leaving two independent Green's functions

$$\begin{aligned} D^R(t,t') &= D^A(t',t) = -i\langle P_{cl}(t)P_q(t')\rangle\,, \\ D^K(t,t') &= -i\langle P_{cl}(t)P_{cl}(t')\rangle. \end{aligned} \tag{47}$$

where D^R and D^A are the retarded and advanced response functions of the oscillator mode, respectively, while D^K is the Keldysh Green's function, which contains information about the temporal correlations and occupancy of the mode. The corresponding Feynman diagrams for these Green's functions are shown in Fig. 7 where the classical and quantum fields are represented by solid and dashed lines, respectively.

A. Saddle-point approach

In order to treat the Keldysh path-integral using saddle-point methods. We are required to vary the forward and backwards time components of the Keldysh contour independently. In the classical limit $\hbar \to 0$, the action on outward and return paths are extremized by the same classical path

$$\lim_{\hbar\to 0}\langle P_\pm(t)\rangle = \mathcal{P}(t), \tag{48}$$

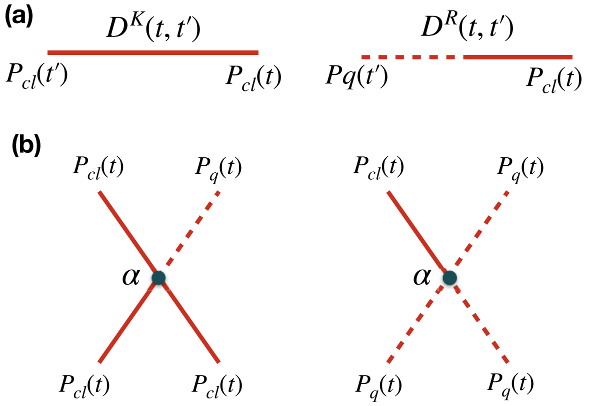

FIG. 7. (a) shows graphical representation of the Green's functions in Keldysh field theory consisting of two kinds of fields, namely the classical field $P_{cl}(t)$ (solid line) and the quantum fields $P_q(t)$ (dashed line). Two independent Green's functions, namely the retarded $D^R(t,t')$ and the Keldysh $D^K(t,t')$ Green's functions, are constructed out of the classical and the quantum fields via Eq. (47). (b) The nonlinearity of the P oscillator mode is shown diagrammatically by the quartic interaction vertices with the coupling strength α. The interaction vertices are odd in the quantum fields required by the causality structure of the two-contour field theory.

so that the outward and return path actions are equal and the Keldysh action on the classical contour is zero, $\mathcal{S}_K[\mathcal{P}] = (\mathcal{S}[P_+] - \mathcal{S}[P_-])|_{P_\pm=\mathcal{P}} = 0$. This means that a variational approach must consider paths where $P_q \neq 0$, for which the Keldysh action is finite [59].

The condition that the Keldysh action is stationary with respect to independent variations of P on the upper and lower contour yields

$$-\frac{\delta\mathcal{S}_K}{\delta P(t)} = \left[\partial_t^2 + \omega_P^2 + m(t)\right]P(t) + \alpha P^3(t) - E(t) = 0, \tag{49}$$

where $P(t)$ lies on either the upper or lower part of the Keldysh contour. This equation of motion defines the classical trajectory $\mathcal{P}(t) = \langle P_{cl}(t)\rangle_{\hbar\to 0}$, which is the saddle point of the Keldysh action. Since the path integral Z_K is invariant under a time-dependent shift of variables, $P \to P + \delta P(t)$, which leaves the measure unchanged $\mathcal{D}[P] = \mathcal{D}[P + \delta P]$,

$$\begin{aligned} 0 &= \int \mathcal{D}[P+\delta P]e^{i\mathcal{S}_K[P+\delta P]/\hbar} - \int \mathcal{D}[P]e^{i\mathcal{S}_K[P]/\hbar} \\ &= \int \mathcal{D}[P]e^{i\mathcal{S}_K[P]/\hbar}\int_C dt\left(\frac{i}{\hbar}\frac{\delta\mathcal{S}_K}{\delta P(t)}\right)\delta P(t), \end{aligned} \tag{50}$$

the equation of motion (49) is exact when averaged over quantum trajectories,

$$\left\langle\frac{\delta\mathcal{S}_K}{\delta P(t)}\right\rangle = \int \mathcal{D}[P]e^{i\mathcal{S}[P]/\hbar}\frac{\delta\mathcal{S}_K}{\delta P(t)} = 0, \tag{51}$$

We should not be surprised, for (49), it is equivalent to eliminating the momentum π from the Heisenberg equations of motion, $(\dot{P} = -(i/\hbar)[H,P] = \pi \Rightarrow \ddot{P} = \dot{\pi} = (i/\hbar)[H,\pi] = -\delta H/\delta P)$. If we take the average of the upper and lower

Keldysh contours, we obtain

$$\big(\partial_t^2+\omega_P^2+m(t)\big)\langle P_{cl}(t)\rangle+\alpha\left\langle\frac{1}{2}(P_+^3+P_-^3)\right\rangle=E(t),\quad(52)$$

where we assume a classical source field $E_\pm(t)=E(t)$. We can expand $(P_+^3+P_-^3)=2P_{cl}^3+(3/2)P_{cl}P_q^2$ and by rewriting the point-split expectation value $\langle P_{cl}P_q^2\rangle\rightarrow\langle T_C\hat{P}_{cl}(t_1)\hat{P}_q(t_2)\hat{P}_q(t_3)\rangle=0$ in terms of time-ordered Heisenberg operators, we find that it vanishes. At the Gaussian level of approximation, this can be understood because $\langle P_q^2P_{cl}\rangle=\langle P_q\rangle\langle P_qP_{cl}\rangle+\langle P_q^2\rangle\langle P_{cl}\rangle$, which vanishes because the first- and second-order moments of P_q vanish, $\langle P_q\rangle=\langle P_q^2\rangle=0$, but in Appendix C, we show that this is true to all orders. It follows that

$$\big(\partial_t^2+\omega_P^2+m(t)\big)\langle P_{cl}(t)\rangle+\alpha\langle P_{cl}(t)^3\rangle=E(t).\quad(53)$$

We calculate the leading quantum fluctuations about the classical trajectory $\langle\delta P_{cl}^2\rangle\sim O(\hbar)$, determined from the leading quadratic expansion of the action about the classical trajectory,

$$\mathcal{S}_G=\int_C dt\,\frac{1}{2}\big[\delta\dot{P}^2-\big(\omega_P^2+m(t)+3\alpha\mathcal{P}^2(t)\big)\delta P^2\big]\quad(54)$$

where $\delta P(t)=P(t)-\mathcal{P}(t)$ is the deviation from the classical path. The cubic term in the equation of motion in Eq. (49) now acquires an additional component from the Wick contractions between the fluctuations,

$$\big\langle P_{cl}^3(t)\big\rangle_{\mathcal{S}_G}\rightarrow\mathcal{P}(t)^3+3\big\langle\delta P_{cl}^2(t)\big\rangle_{\mathcal{S}_G}\mathcal{P}(t).\quad(55)$$

This introduces a self-energy correction to the oscillator mass

$$m(t)\rightarrow m(t)+\Sigma(t),\quad(56)$$

where

$$\Sigma(t)=3\alpha\big\langle\delta P_{cl}^2(t)\big\rangle_{\mathcal{S}_G}=3i\alpha D_K(t,t)\quad(57)$$

is written in terms of the Keldysh Green's function $D_K(t,t')=-i\langle\delta P_{cl}(t)\delta P_{cl}(t')\rangle_{\mathcal{S}_G}$. The self-energy correction to the mass modifies the equation of motion,

$$\ddot{\mathcal{P}}(t)+\big(\omega_P^2+m(t)+\Sigma(t)\big)\mathcal{P}(t)+\alpha\mathcal{P}(t)^3=E(t).\quad(58)$$

Note that while the fluctuations are Gaussian, the classical equations of motion are nonlinear in α. One of the key effects of this self-energy correction, is a shift in in the paraelectric to ferroelectric critical point.

B. Keldysh action

We now re-interpret these results diagrammatically. The Keldysh action can be divided into Gaussian and quartic components, $\mathcal{S}_K=\mathcal{S}_2+\mathcal{S}_4$. In the classical-quantum basis,

$$\mathcal{S}_2=\frac{1}{2}\int_{-\infty}^{\infty}dt\big(P_{cl}(t),\quad P_q(t)\big)\begin{bmatrix}0 & D_A^{-1}\\ D_R^{-1} & D_K^{-1}\end{bmatrix}\begin{pmatrix}P_{cl}(t')\\ P_q(t')\end{pmatrix}+\int_{t_0}^{\infty}dt P_q(t)E(t),\quad(59)$$

where the noninteracting inverse Green's functions are

$$D_{R,A}^{-1}=(i\partial_t\pm i0^+)^2-(\omega_P^2+m(t)),\quad(60)$$

while D_K^{-1} is a purely imaginary term which sets the thermal boundary conditions. The quartic term

$$\begin{aligned}\mathcal{S}_4&=-\frac{\alpha}{4}\int_{t_0}^{\infty}dt\big[P_+^4(t)-P_-^4(t)\big]\\&=-\alpha\int_{t_0}^{\infty}dt\big[P_{cl}^3(t)P_q(t)+(1/4)P_q^3(t)P_{cl}(t)\big],\end{aligned}\quad(61)$$

only contains terms with odd powers of P_q, as shown in Fig. 7. This is the starting point for the diagrammatic expansions. The expectation value $\langle P_{cl}(t)\rangle_{\mathrm{S_{eff}}}$ can be expanded perturbatively in powers of the coupling strength α as

$$\begin{aligned}\langle P_{cl}(t)\rangle_{S_K}&=\int D[P]\,e^{i(\mathcal{S}_2+\mathcal{S}_4)}P_{cl}(t)\\&=\langle P_{cl}(t)\rangle_{\mathcal{S}_2}+i\langle P_{cl}(t)\mathcal{S}_4\rangle_{\mathcal{S}_2}\\&\quad-\frac{1}{2}\langle P_{cl}(t)(\mathcal{S}_4)^2\rangle_{\mathcal{S}_2}+\cdots,\end{aligned}\quad(62)$$

where the expectation values are evaluated with respect to the Gaussian action $\mathcal{S}_2$ (59). The Wick expansion of these terms involves the contraction of pairs of P fields into propagators and contractions of P fields with the external field E, giving rise to a series of Feynman diagrams, as shown in Fig. 8. The contraction of P_{cl} with the external field in the first term defines the linear response

$$\langle P_{cl}(t)\rangle_{\mathcal{S}_2}=-\int dt_1D^R(t,t_1)E(t_1),\quad(63)$$

represented by a solid (classical) line ending at a cross representing the electric field. Wick contractions of the second term in (62) generate two sets of diagrams: a "tree diagram", involving three contractions of P_{cl} with the external field, and a "Hartree diagram," involving the contraction of two P_{cl} fields.

Next, we organize the higher order diagrams in Fig. 8 into two classes: (a) "tree diagrams" with a maximum number of classical fields contracted with the external electric fields $E(t)$ and (b) Hartree diagrams (unshaded in Fig. 8) where a pair (or more) of classical fields are contracted among themselves, forming a loop which does not contain $E(t)$. An example of the first class of diagrams is shown by the gray shaded diagram in Fig. 8. These diagrams have maximum power of the electric field at a given order of the perturbation series and contain only the interaction vertices with three classical fields and only 1 quantum field. The second class of diagrams involve the scattering off quantum fluctuations . These scattering processes describe the self-energy corrections to the mass of the soft polar mode by quantum fluctuations, and can contain retarded and Keldysh Green's functions.

In Fig. 9(a), we show that a resummation of the tree-diagrams leads to the classical EOM, whose solution is denoted $\mathcal{P}(t)$ [also given in Eq. (31)]. To understand the resummation, we start with the first-order diagram in Fig. 9 (same as the gray shaded diagram in Fig. 8), where each of the three classical fields of the interaction vertex are contracted with $E(t)$, yielding $(\langle P_{cl}\rangle_{\mathrm{S}_2})^3$. Higher order diagrams can be understood as the result of adding further "tree corrections" to each external line. The resummation of these diagrams nonperturbative classical solution can then be rewritten in

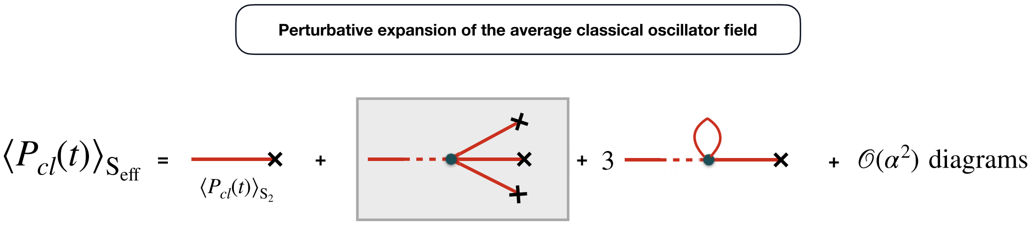

FIG. 8. Diagrammatic expansion for the expectation of the classical component of the oscillator field: obtained by expanding the quartic interaction term in the effective action $\mathcal{S}_{\rm eff}$ in powers of the coupling strength α. The first term in the right-hand side (shown by a solid line ending at a cross) is the expectation value for the noninteracting oscillator given in Eq. (63). Among the first-order diagrams, the shaded diagram contains maximum influence from the external electric field at this order of perturbation series while the unshaded diagram contains loops of classical fields independent of $E(t)$. The former kind of diagrams form the "tree series" (see Fig. 9) leading to classical EOM while the latter kind incorporates effects of quantum fluctuations in the dynamics that can not be captured within the classical theory.

terms of Green's functions as

$$\mathcal{P}(t) = -\int_{t_0}^{\infty} dt_1 D^R(t,t_1)(E(t_1) - \alpha\mathcal{P}(t_1)^3). \tag{64}$$

This classical solution is represented diagrammatically by a solid line ending at the symbol C in Fig. 9. This identification of the tree series as "classical" diagrams is crucial to identify and study the quantum effects near the PE-FE transition which we discuss next.

C. Perturbative quantum corrections

In this section, we will study the leading quantum correction to the soft-mode mass, determining the resulting shift in the critical point, first for the case of single phonon mode (single nonlinear oscillator) in Sec. IV C 1, generalizing the calculation to the multimode case in Sec. IV C 2.

1. Single phonon mode

Quantum corrections to the classical equations of motion are obtained by inserting self-energy corrections to the retarded propagator. The leading Hartree self-energy correction is derived from the one-loop retarded self-energy $\Sigma^R(t)$, corresponding to the Hartree approximation, as shown in Fig. 10. Within this approximation $\Sigma^R(t,t') = \Sigma(t)\delta(t-t')$ is local in time so that quantum fluctuations manifest themselves as a time-dependent modification of the oscillator mass (see Appendix B for more details),

$$m(t) \to m(t) + \Sigma(t) \tag{65}$$

in Eq. (4), where

$$\Sigma(t) = 3\alpha\langle\delta P_{cl}(t)^2\rangle_{S_G} \tag{66}$$

is proportional to the fluctuations in $P_{cl}(t)$ calculated using the Gaussian correction to the action,

$$\mathcal{S}_G = \int_C dt\frac{1}{2}\big[\delta\dot{P}^2 - \big(\omega_P^2 + m(t) + 3\alpha\mathcal{P}^2(t)\big)\delta P^2\big] \tag{67}$$

However, if we restrict ourselves to the "paraelectric phase" where $\mathcal{P}(t) = \langle P_{cl}(t)\rangle = 0$, then in this case, the $3\alpha\mathcal{P}^2(t)$ term vanishes in $\mathcal{S}_G$. This does not restrict our consideration since in this section the main effect of the driving is incorporated in $m(t)$. The Gaussian action then coincides with the quadratic action $\mathcal{S}_G \equiv \mathcal{S}_2$ and the quantum corrections are the perturbative Hartree corrections, i.e.,

$$\Sigma(t) = 3\alpha\langle\delta P_{cl}(t)^2\rangle_{S_2} \quad (\mathcal{P}(t) = 0). \tag{68}$$

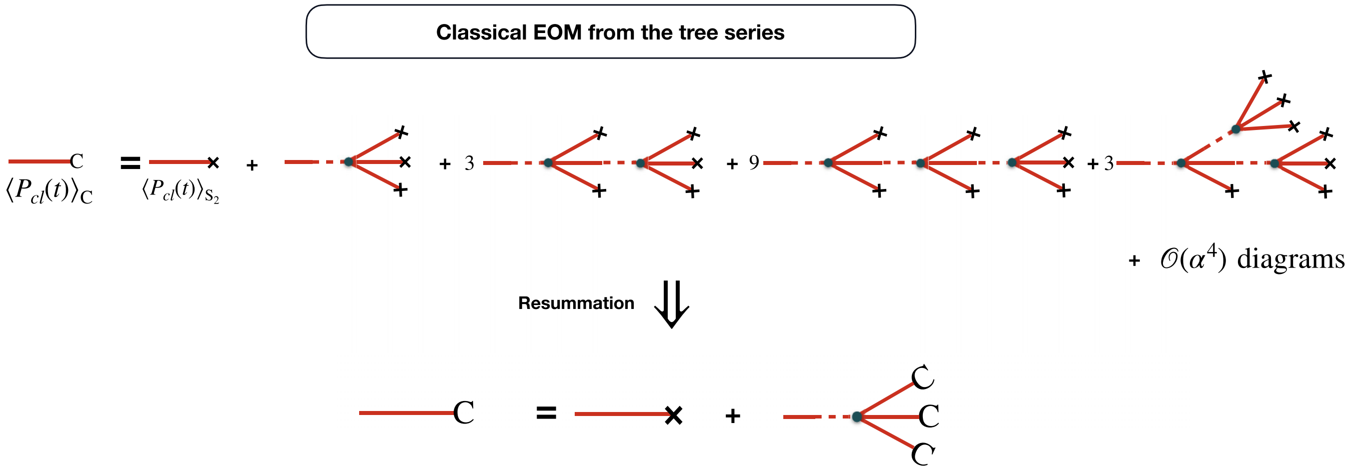

FIG. 9. (a) Recovery of the classical limit from Keldysh field theory: the solution of the classical EOM [see Eq. (31)] $\langle P_{cl}\rangle_{\rm C}(t)$ is obtained from the full expectation value $\langle P_{cl}(t)\rangle_{S_{\rm eff}}(t)$ by restricting the sum only to the "tree diagrams" shown here. These are the diagrams which contain maximum powers of the external electric field, symbolically represented by a cross mark here, in each order of the perturbation theory. These diagrams can be regrouped to yield the nonperturbative classical solution.

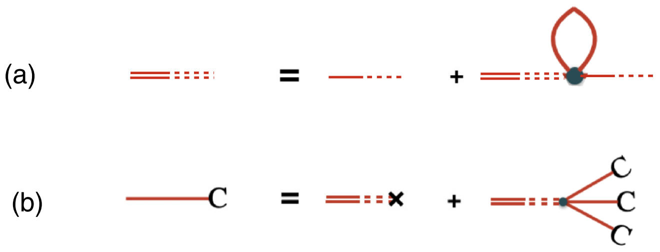

FIG. 10. (a) Hartree self-energy insertion to the retarded propagator, describing the leading $O(\hbar)$ effect of quantum fluctuations. (b) The equation of motion now involves the renormalized propagator.

The quantum contribution to the self-energy is determined from the equal-time Keldysh propagator so that

$$\Sigma(t) = 3\alpha i D^K(t,t). \tag{69}$$

Next, we calculate the equal time Keldysh Green's function $D^K(t,t)$ for the noninteracting harmonic oscillator with a time-dependent mass $\omega_P^2 + m(t)$. To do so, we rewrite the Keldysh Green's functions in terms of the Heisenberg position operators of the Harmonic oscillator,

$$D_K(t,t') = -i\langle P_{cl}(t)P_{cl}(t')\rangle = -\frac{i}{2}\langle\{\hat{P}(t),\hat{P}(t')\}\rangle. \tag{70}$$

Consider a noninteracting oscillator with time-dependent mass $\omega^2(t) = \omega_P^2 + m(t)$, where $m(0) = 0$ and Hamiltonian

$$H = \frac{1}{2}(\hat{\pi}^2 + \omega^2(t)\hat{P}^2). \tag{71}$$

Here $\hat{P}$ and $\hat{\pi}$ are canonical position and momentum operators, respectively. We now calculate $D_K(t,t')$ from the expectation value of the Heisenberg operators $P(t)$, evaluated in the initial state. We can relate the Heisenberg Schrödinger operators $P = P(0)$ and $\pi = \pi(0)$ by

$$\hat{P}(t) = a(t)\hat{P} + b(t)\hat{\pi}. \tag{72}$$

From the equations of motion $\partial_t\hat{P}(t) = \hat{\pi}(t)$ and $\partial_t\hat{\pi}(t) = -\omega^2(t)\hat{P}(t)$, we deduce that $\partial_t^2 P(t) = -\omega^2(t)P(t)$, so the coefficients $a(t)$ and $b(t)$ satisfy the differential equation

$$\left[\partial_t^2 + \omega_P^2 + m(t)\right]\begin{pmatrix} a(t) \\ b(t)\end{pmatrix} = 0, \tag{73}$$

subject to the boundary conditions

$$\begin{pmatrix} a(0) \\ b(0)\end{pmatrix} = \begin{pmatrix} 1 \\ 0\end{pmatrix}, \quad \begin{pmatrix} \dot{a}(0) \\ \dot{b}(0)\end{pmatrix} = \begin{pmatrix} 0 \\ 1\end{pmatrix}, \tag{74}$$

The Keldysh Green's function for a system initially in the state $|n\rangle$ with n phonons, can then be evaluated as

$$\begin{aligned} D_K(t,t') &= -\frac{i}{2}\langle n|\{\hat{P}(t),\hat{P}(t')\}|n\rangle \\ &= -i[a(t)a(t')\langle n|P^2|n\rangle + b(t)b(t')\langle n|\pi^2|n\rangle] \\ &= -i\left[a(t)a(t') + \omega_P^2 b(t)b(t')\right]\left(\frac{n+\frac{1}{2}}{\omega_P}\right), \end{aligned} \tag{75}$$

so that

$$\langle P_{cl}^2(t)\rangle = \left(a^2(t) + \omega_P^2 b^2(t)\right)\left(\frac{n+\frac{1}{2}}{\omega_P}\right). \tag{76}$$

As an example, consider a linear time dependence in the mass of the form $m(t) = -\omega_P^2(t/t_0)$ for which the oscillator undergoes a quantum phase transition as $t \to t_0$ (at the bare level without self-energy corrections). We can obtain an analytical solution from Eq. (73) and in the extreme limits, this leads to simple form of the quantum correction (see Appendix D for more details) given by

$$\Sigma(t) = \begin{cases} \frac{3\alpha}{2\sqrt{\omega_P^2 + m(t)}}, & \omega_P \gg 1/t_0, \\ \frac{3\alpha}{2\omega_P}\left(1 + \frac{t^3\omega_P^2}{3t_0}\right), & \omega_P \ll 1/t_0, \end{cases} \tag{77}$$

where the initial state of the oscillator is chosen to be the vacuum state $n = 0$. In the next section, we will extend this analysis to the case of interacting phonons with different momenta and study experimentally measurable effects of the quantum fluctuations in the dynamics.

2. *Interacting phonons in 3D*

We now extend the discussion to the higher dimensional case where the soft-phonon mode develops dispersion. As an illustration, consider 3D phonons with dispersion

$$\omega_k^2(t) = {\omega_P}^2 + m(t) + (ck)^2 \tag{78}$$

with an ultraviolet momentum cutoff Λ of the slow mode arising from an underlying lattice. We further assume that the separation of the energy scales between the slow P modes and the fast Q modes is valid at all momenta, i.e. $c\Lambda \ll \Omega$. This allows us to extend the effective potential approach for slow phonon modes described in (30) to the multimode (P modes) case, where the resonantly driven Q modes only result in a time-dependent potential for P modes modifying the bare mass ${\omega_P}^2 \to \omega_P^2 + m(t)$.

The quantum correction can be calculated from $\Sigma(t) = \int_{\vec{k}}\Sigma(\omega_k)$ where $\int_{\vec{k}} = \int d\vec{k}/(2\pi)^3$ and $\Sigma_q^R(\omega_k)$ is the retarded self-energy for the independent oscillator modes of frequency $\omega_k^2(t)$ (78),

$$\Sigma(\omega_k) = 3\alpha\frac{\left[a^2(k,t) + \left(\omega_P^2 + c^2k^2\right)b^2(k,t)\right]}{\sqrt{\omega_P^2 + c^2k^2}}\left(n + \frac{1}{2}\right), \tag{79}$$

where the coefficients $a(k,t)$ and $b(k,t)$ are calculated from Eq. (73) replacing $\omega_P^2 + m(t)$ by $\omega_k^2(t)$. Unless otherwise mentioned the initial state of the oscillators is chosen to be the vacuum state $n = 0$.

Before understanding the effects quantum fluctuations in the dynamics, we first focus on the equilibrium quantum correction $\Sigma(\sqrt{\omega_P^2 + (ck)^2})$ at $t = 0$. This modifies the bare mass of the oscillators from $\omega_k^2(t=0)$ to $\tilde{\omega}_k^2(t=0)$ given by

$$\tilde{\omega}_k^2(t=0) = \left[\omega_P^2 + (ck)^2 + \int_{\vec{k}}\Sigma\left(\sqrt{\omega_P^2 + (ck)^2}\right)\right]. \tag{80}$$

Here, we note that $\int_{\vec{k}}\Sigma(\sqrt{\omega_P^2+(ck)^2})$ is ultraviolet divergent ($\propto \Lambda^2\alpha/c$) and leads to a cut-off dependent shift of the zero-point energy of the oscillator. This divergence can be renormalized by a redefinition of the oscillator energy ω_P^2 by $\tilde{\omega}_P^2=\omega_P^2+\int_{\vec{k}}\Sigma(\sqrt{\omega_P^2+(ck)^2})\approx\omega_P^2+3\alpha\Lambda^2/(8\pi^2c)$. $\tilde{\omega}_P$ is the experimentally measurable energy of the phonon in equilibrium.

As time evolves, the dynamical quantum correction modifies the energy of the slow mode as

$$\tilde{\omega}_k^2(t)=\omega_P^2+(ck)^2+m(t)+\int_{\vec{k}}\Sigma(\omega_k(t)). \tag{81}$$

To clearly differentiate between the Λ-dependence appearing in the equilibrium zero-point energy of the P mode from the relevant dependence appearing in the dynamical quantum fluctuations, we rewrite the above equation as

$$\tilde{\omega}_k^2(t)=\left[\tilde{\omega}_P^2+(ck)^2\right]+m(t)+\int_{\vec{k}}\left[\Sigma(\omega_k(t))-\Sigma_q^R\left(\sqrt{\omega_P^2+(ck)^2}\right)\right]. \tag{82}$$

Here, the first term of Eq. (82) corresponds to the dispersion of the oscillator at ($t=0$) modified by the equilibrium quantum correction. The subsequent terms corresponds to the change in the oscillator energy at later time t (compared to that at $t=0$). These terms consist of (a) an explicit time-dependence through $m(t)$ induced by the external drive and (b) the change in the quantum self-energy (nonequilibrium quantum correction) $\delta\Sigma(t)=\int_{\vec{k}}[\Sigma(\omega_k(t))-\Sigma(\omega_k(t=0))]$. By this rearrangement, we eliminate the equilibrium ultraviolet divergences from the time-dependent part of the oscillator energy [the second line of Eq. (82)]. It is useful to recast Eq. (82) in a form that does not include the unobservable bare phonon energy ω_P, replacing the bare ω_P^2 with the experimentally measurable $\tilde{\omega}_P^2$ in $\delta\Sigma(t)$ as,

$$\begin{aligned}\tilde{\omega}_k^2(t)\approx{}&\left[\tilde{\omega}_P^2+(ck)^2\right]+m(t)\\&+\int_{\vec{k}}\left[\Sigma\left(\sqrt{\tilde{\omega}_P^2+(ck)^2+m(t)}\right)\right.\\&\left.-\Sigma(\sqrt{\tilde{\omega}_P^2+(ck)^2})\right],\end{aligned} \tag{83}$$

which leads to corrections of higher order in α. Indeed, replacing ω_P^2 by $\tilde{\omega}_P^2$ leads to $\mathcal{O}(\alpha^2)$ change in $\delta\Sigma(t)$. As the leading order answer is $\mathcal{O}(\alpha)$, this effect can be neglected.

The nonequilibrium quantum correction leads us to predict a shift in the critical fluence. To model this phenomenon, we model the effect of a time-dependent pump by $m(t)=-\tilde{\omega}_P^2t/t_0$ corresponding to a linearly increasing fluence. In the absence of quantum corrections, the frequency would go to zero at $t=t_0$. To evaluate the effects of quantum fluctuations, we solve $\tilde{\omega}_k^2(t_0^q)=0$ from Eq. (83) numerically to determine the shift in the critical time. In Fig. 11, we show the ratio of the shifted and bare critical times t_0^q/t_0 as a function of the rate of driving in the dimensionless unit $\tilde{\omega}_Pt_0$ for three different values of the quartic coupling, $\alpha=0.03,\ 0.07,\ \text{and}\ 0.1$.

In the quantum quench limit, the system is driven to the QCP so rapidly that system is unable adjust to the QCP ($1/\tilde{\omega}_P\gg t_0$ and $1/(c\Lambda)\gg t_0$); in this case the dynamical quantum corrections are expected to be small. Using the analytical form given in Eq. (77) for the single mode case and generalizing it for the multimode case, we obtain an estimate of the quantum correction in the mass (in the limit $1/c\Lambda\gg t_0$ and $\tilde{\omega}_P\ll c\Lambda$),

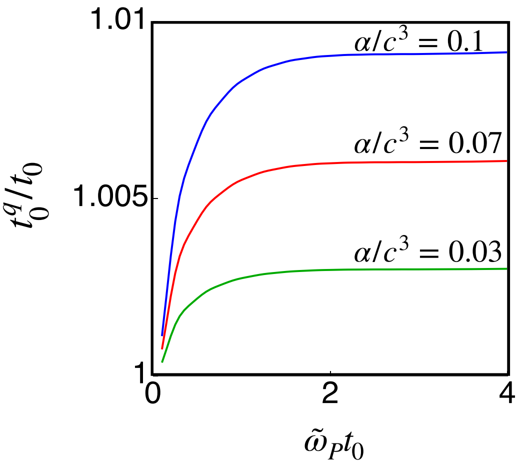

FIG. 11. Shift in the critical point due to quantum fluctuations: the ratio between the critical time with quantum fluctuations and the classical critical time t_0^q/t_0 is plotted as a function of the rate of pumping expressed in the dimensionless unit $\tilde{\omega}_Pt_0$ for three different strengths of the nonlinearity (in dimensionless unit) $\alpha/c^3=0.03,\ 0.07,\ \text{and}\ 0.1$. In the fast pumping limit $\tilde{\omega}_Pt_0\ll1$, t_0^q grows from t_0 as t_0^2 with increasing t_0. This growth saturates in adiabatic limit $\tilde{\omega}_Pt_0\gg1$ recovering the signatures of quantum criticality. We choose $c^2\Lambda^2/\tilde{\omega}_P^2=100$ to set the ultraviolet cutoff Λ.

$$\delta\Sigma(t)\approx3\frac{\alpha}{16\pi^2c^3}\frac{t^3}{3t_0}c^4\Lambda^4. \tag{84}$$

The above contribution from the nonequilibrium quantum correction is small for $t\sim t_0$ by $1/(c\Lambda)\gg t_0$. To find out the shift in the critical time, we solve

$$\tilde{\omega}_P^2\left[1-\frac{t_0^q}{t_0}\right]+\delta\Sigma\left(t_0^q\right)=0. \tag{85}$$

In the quantum quench limit, the leading order deviation of t_0^q from t_0 is obtained from the above equation by replacing $\delta\Sigma(t_0^q)$ by $\delta\Sigma(t_0)$ to obtain

$$\frac{t_0^q}{t_0}\approx1+\frac{\alpha}{16\pi^2c^3}\tilde{\omega}_P^2t_0^2\left(\frac{c^4\Lambda^4}{\tilde{\omega}_P^4}\right). \tag{86}$$

Thus the leading order deviation of t_0^q from t_0 grows as t_0^2 as we increase the sweeping time t_0.

When the system is driven to the QCP slowly, the system has a longer time to adjust to the QCP and the effects of quantum corrections become marked (see Fig. 11). In the adiabatic regime $\tilde{\omega}_Pt_0\gg1$, the quantum correction to the retarded self-energy takes the form

$$\Sigma(t)\approx3\frac{\alpha}{8\pi^2c}\Lambda^2\left[1-\frac{\left[\tilde{\omega}_P^2+m(t)\right]}{c^2\Lambda^2}\ln\left(\frac{c^2\Lambda^2}{\left[\tilde{\omega}_P^2+m(t)\right]}\right)\right], \tag{87}$$

where we neglected the terms of $O(1)$ as small in comparison with the logarithm in the second term. As discussed above, the first term in (87) can be absorbed in a renormalization of the equilibrium parameters, leading to an increase in the mode frequency due to

$$\delta\Sigma(t) = 3\frac{\alpha}{8\pi^2 c}\left[\frac{\tilde{\omega}_P^2}{2c^2}\ln\left(\frac{c^2\Lambda^2}{\tilde{\omega}_P^2}\right) - \frac{[\tilde{\omega}_P^2 + m(t)]}{2c^2}\ln\left(\frac{c^2\Lambda^2}{[\tilde{\omega}_P^2 + m(t)]}\right)\right]. \tag{88}$$

The resulting correction has a weak logarithmic dependence on Λ, consistent with a system at its the upper critical dimension, demonstrating that in the adiabatic limit we recover the signatures of equilibrium quantum criticality.

In the adiabatic limit, the leading order deviation of t_0^q from t_0 is obtained from Eq. (85) by replacing $\delta\Sigma(t_0^q)$ by $\delta\Sigma(t_0)$ to obtain

$$t_0^q = t_0\left[1 + 3\frac{\alpha\tilde{\omega}_P^2}{16\pi^2 c^3}\ln\left(\frac{c^2\Lambda^2}{\tilde{\omega}_P^2}\right)\right]. \tag{89}$$

We have computed an additional delay in the transition to the polar phase due to leading order quantum fluctuations. Since here we are considering a model where the fluence varies linearly in time, this result corresponds to an increase in the critical fluence. More generally quantum fluctuations increase the renormalized mass, thus requiring modified fluence profiles for the system to transition to the polar ordered state. Therefore the dependence of the critical fluence on the driving rate can be used to identify and to characterize quantum corrections in driven ferroelectrics.

V. SUMMARY

In this work, we have analyzed a model of a driven lattice system close to a ferroelectric instability. We have shown that classically, the driving can be described as a modification of the nonlinear phonon potential leading to a phase transition beyond a critical fluence. The structure of the ordered phase can be tuned by light polarization. For fluence above the critical one, a second phase transitions is possible that breaks additional symmetries. A further increase in fluence beyond a second critical value suppresses the ordered phase and in some cases, leads to a chaotic behavior. Beyond classical dynamics, we demonstrated that the classical equations of motion arise as a approximation to the full quantum Keldysh evolution and identified the lowest-order quantum corrections. The latter effects predict a dependence of the critical fluence on the driving rate, which may be observable experimentally.

ACKNOWLEDGMENTS

We acknowledge stimulating discussions with G. Aeppli, A.V. Balatsky, J. Flick, W.Hu and M. Kulkarni. Z.Z., and P.Ch. are funded by DOE Basic Energy Sciences grant DE-SC0020353 and P. Co. is supported by NSF Grant No. DMR-1830707. A. C. is a Rutgers Center for Materials Theory Abrahams Fellow as was P.A.V. during his time at Rutgers when this project was initiated.

APPENDIX A: EFFECTS OF NONBIQUADRATIC *P-Q* INTERACTIONS

In this Appendix, we illustrate the reasons why nonbiquadratic P-Q interaction terms, such as PQ, PQ^3, and P^3Q, do not lead to qualitatively new effects and can be neglected. To start, we consider the two-oscillator model in Sec. III C with additional action

$$S_{\text{odd}} = \int dt\left[\gamma_{11}PQ + \frac{\gamma_{13}}{2}PQ^3 + \frac{\gamma_{31}}{2}P^3Q\right]. \tag{A1}$$

The classical EOM (27) then become

$$\ddot{Q} + \omega_Q^2 Q + \beta_1\dot{Q} - \gamma P^2 Q - \frac{3\gamma_{13}}{2}PQ^2 - \frac{\gamma_{31}}{2}P^3 - \gamma_{11}P = Z_q E(t), \tag{A2}$$

$$\ddot{P} + \omega_P^2 P + \beta_0\dot{P} - \gamma Q^2 P + \alpha P^3 - \frac{\gamma_{13}}{2}Q^3 - \frac{3\gamma_{31}}{2}P^2 Q - \gamma_{11}Q = Z_p E(t). \tag{A3}$$

If we first neglect the backaction terms in Eq. (A2), namely the terms involving Ps, then in this approximation, we can apply (28), namely,

$$Q(t) = \chi_q E_0\cos(\Omega t), \tag{A4}$$

where χ_q is defined in the main text. With this substitution, the Q and Q^3 terms in Eq. (A3) can be directly absorbed into a time-dependent renormalization of the electric field,

$$\tilde{E}(t) = E(t) + \frac{\gamma_{13}}{8Z_p}(\chi_q E_0)^3(\cos 3\Omega t + 3\cos\Omega t) + \frac{\gamma_{11}}{Z_p}\chi_q E_0\cos(\Omega t). \tag{A5}$$

The additional two terms do not lead to any qualitatively new physics. The second term simply renormalizes the oscillating electric field at frequency Ω, while the first one introduces oscillations at 3Ω that are even further off-resonance for the P mode. In addition, in the main text we have demonstrated that the critical E_0 for the light-induced transition scales with ω_P [see, e.g., Eq. (21)] and is therefore small for a system close to the phase transition. In that regime, one can also justify the neglect of higher order terms in E_0 due to the smallness of E_0. The P^2Q term in (A3) corresponds to a time-dependent cubic potential for P in the original action (A1). This term averages to zero over a period $2\pi/\Omega$ and is therefore unimportant in the paraelectric phase. In the ferroelectric phase, using the method we used to derive Eq. (33), we can replace P^2 by P_0^2 allowing this term to also be absorbed into an effective electric field

$$\tilde{\tilde{E}}(t) = \tilde{E}(t) + \chi_q E_0\frac{3\gamma_{31}}{2}P_0^2\cos(\Omega t). \tag{A6}$$

We do not expect the omission of the backaction terms in Eq. (A2) to change our arguments qualitatively, because the P^2Q term merely results in a shift of the resonant frequency of the Q mode, while the other backaction terms can be absorbed into an additional renormalization of the electric field, using similar arguments to those presented above.

To verify these arguments directly, Figs. 12(a) and 12(b) show the numerical solutions of Eqs. (A2) and (A3).

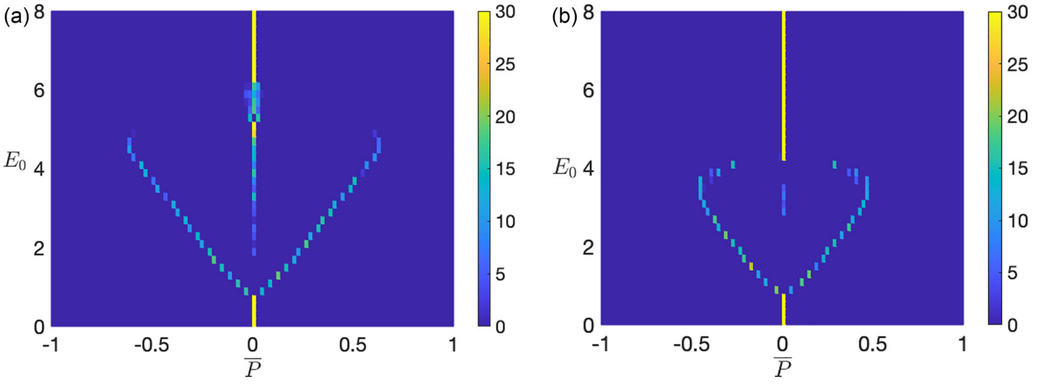

FIG. 12. Time-averaged polarization $\overline{P}$ vs electric field strength E_0 including nonbiquadratic P-Q interactions [Eqs. (A2) and (A3)]. These results were obtained from 30 random initial conditions at each fixed E_0, and the color of grids indicates the number of times the system reaches $\overline{P}$ in its steady state. The common parameter values for these plots are $\omega_P = 0.1$, $\omega_Q = 2$, $\Omega = 2.1$, $\gamma = 0.01$, $Z_q = 1$, $Z_p = 0.3$, $\alpha = 1$, and $\beta_1 = \beta_0 = 0.1$. We choose (a) $\gamma_{13} = \gamma_{31} = 0.003$ and (b) $\gamma_{13} = \gamma_{31} = 0.01$.

Comparing them to Fig. 4(f), we see that the inclusion of nonbiquadratic terms hardly affects the onset of ferroelectricity, although it can lead to quantitative differences at higher fields. However, we note that the qualitative features, such as multiple coexisting solutions and chaotic behavior, still persist when these terms are included.

APPENDIX B: TWO-TIME CORRELATIONS IN QUANTUM CORRECTIONS

In the main text, we have perturbatively calculated the quantum corrections to the classical EOM $\langle P_{cl}\rangle_C(t)$ of the oscillator given in Eq. (64) by modifying the mass of the polar mode $m(t)$ in Eq. (65). In this Appendix, we present the details of calculations leading to this result. In particular, we show that in the lowest order (the one which we consider), two-time correlations and noise terms do not arise from quantum corrections.

The quantum correction is obtained via the retarded self-energy Σ^R which can in general is a function of two times, $\Sigma^R(t,t')$ [43,44]. However, if we calculate $\Sigma^R(t,t')$ within a Hartree appproximation, i.e., restricting ourselves to lowest order diagrams (Fig. 13), the retarded self-energy becomes local in time, $\Sigma(t,t') = \Sigma^R(t)\delta(t-t')$ [57]. The Keldysh self-energy $\Sigma^K(t,t')$ (Fig. 13, right) which typically introdues noise in the dynamics (see Sec. 11.3 of the Ref. [59]), vanishes within a Hartree aprroximation due to causality structure of the equal-time Green's functions $D^R(t,t) = 0$. Thus, within the Hartree approximation, we may write the nonequilibrium Dyson equation for the interacting retarded Green's function as [57]

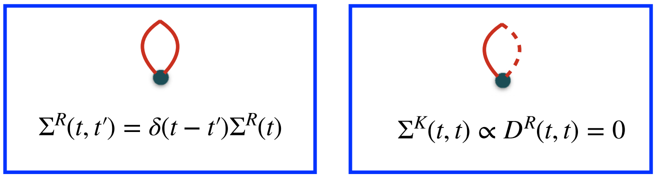

FIG. 13. Diagrams for retarded and Keldysh self-energy within Hartree approximation are shown. At the one-loop order, the retarded self-energy is a frequency independent one-time object $\Sigma^R(t)$ while the Keldysh component vanishes due to the causality structure of the equal time Green's functions.

$$D^R_{int}(t,t') = D^R(t,t') + \int D^R(t,t_1)\Sigma^R(t_1)D^R_{int}(t_1,t'). \quad \text{(B1)}$$

Inverting the above equation by applying D^{-1R} from the left and D^{-1R}_{int} from the right we obtain

$$\begin{aligned} D^{-1R}_{int}(t,t') &= D^{-1R}(t,t') - \delta(t-t')\Sigma^R(t') \\ &= \delta(t-t')\big[-\partial_t^2 - \big(\omega_P^2 + m(t) + \Sigma^R(t)\big)\big]. \end{aligned} \quad \text{(B2)}$$

In this way, the quantum corrections in the Hartree approximation appear as a modification in the time dependence of the mass of the polar mode.

APPENDIX C: PROOF THAT $\langle P_q^2 P_{cl}\rangle = 0$.

To prove the identity $\langle P_q^2 P_{cl}\rangle = 0$ we consider the point-split relation $\langle P_q(t+\delta)P_q(t)P_{cl}(t-\delta)\rangle$, which we rewrite as a path-ordered expectation value of the corresponding Heisenberg operators

$$\begin{aligned} &\langle P_q(t+\delta)P_q(t)P_{cl}(t-\delta)\rangle \\ &= \frac{1}{2}\langle \mathcal{T}_C(\hat{P}_+(t+\delta) - \hat{P}_-(t+\delta))(\hat{P}_+(t) - \hat{P}_-(t))(\hat{P}_+(t-\delta) \\ &\quad + \hat{P}_-(t-\delta))\rangle. \end{aligned} \quad \text{(C1)}$$

where $\mathcal{T}_C$ denotes ordering along the Keldysh contour. We now expand this into eight terms, noting that (i) operators on the lower $(-)$ contour occur after operators on the upper contour $(+)$, (ii) operators on the upper contour are time-ordered (iii) operators on the lower contour are reverse-time ordered. Thus since $t+\delta > t > t-\delta$,

$$\begin{aligned} \langle \mathcal{T}_C\hat{P}_+(t+\delta)\hat{P}_+(t)\hat{P}_+(t-\delta)\rangle &= \langle \hat{P}(t+\delta)\hat{P}(t)\hat{P}(t-\delta)\rangle \\ \langle \mathcal{T}_C\hat{P}_+(t+\delta)\hat{P}_+(t)\hat{P}_-(t-\delta)\rangle &= \langle \hat{P}(t-\delta)\hat{P}(t+\delta)\hat{P}(t)\rangle \\ -\langle \mathcal{T}_C\hat{P}_+(t+\delta)\hat{P}_-(t)\hat{P}_+(t-\delta)\rangle &= -\langle \hat{P}(t)\hat{P}(t+\delta)\hat{P}(t-\delta)\rangle \\ -\langle \mathcal{T}_C\hat{P}_+(t+\delta)\hat{P}_-(t)\hat{P}_-(t-\delta)\rangle &= -\langle \hat{P}(t-\delta)\hat{P}(t)\hat{P}(t+\delta)\rangle \\ -\langle \mathcal{T}_C\hat{P}_-(t+\delta)\hat{P}_+(t)\hat{P}_+(t-\delta)\rangle &= -\langle \hat{P}(t+\delta)\hat{P}(t)\hat{P}(t-\delta)\rangle \end{aligned}$$

$$\begin{aligned} -\langle \mathcal{T}_C \hat{P}_-(t+\delta)\hat{P}_+(t)\hat{P}_-(t-\delta)\rangle &= -\ \langle \hat{P}(t-\delta)\hat{P}(t+\delta)\hat{P}(t)\rangle \\ \langle \mathcal{T}_C \hat{P}_-(t+\delta)\hat{P}_-(t)\hat{P}_+(t-\delta)\rangle &= \langle \hat{P}(t)\hat{P}(t+\delta)\hat{P}(t-\delta)\rangle \\ \langle \mathcal{T}_C \hat{P}_-(t+\delta)\hat{P}_-(t)\hat{P}_-(t-\delta)\rangle &= \langle \hat{P}(t-\delta)\hat{P}(t)\hat{P}(t+\delta)\rangle. \end{aligned} \tag{C2}$$

We see that the first and fifth, second and sixth, third and seventh and fourth and eighth terms cancel one another, so that the total sums to zero.

APPENDIX D: DERIVATION OF QUANTUM SELF-ENERGY FOR A SINGLE-MODE PHONON

In the main text, we calculated the quantum correction in the form of Hartree self-energy $\Sigma(t)$ in Eq. (77) for a single-mode phonon. Here we will derive $\sigma(t)$ starting from the formulation to calculate Keldysh Green's function of a harmonic oscillator with time-dependent frequency given in Eq. (75). The Hartree self-energy,

$$\Sigma(t) = 3\alpha i D^K(t,t) = \frac{3\alpha}{2\omega_P}\big(a^2(t) + \omega_P^2 b^2(t)\big). \tag{D1}$$

We solve the differential equations given in Eq. (73) to obatin the solutions with $z = \omega_P t_0$,

$$\begin{aligned} a^2(t) = \pi^2\bigg[&Ai'(-z^{2/3})Bi\bigg\{\bigg(1-\frac{t}{t_0}\bigg)z^{2/3}\bigg\} \\ &- Bi'(-z^{2/3})Ai\bigg\{-\bigg(1-\frac{t}{t_0}\bigg)z^{2/3}\bigg\}\bigg]^2, \end{aligned}$$

$$\begin{aligned} b^2(t) = \pi^2 z^{2/3}\bigg[&Ai(-z^{2/3})Bi\bigg\{-\bigg(1-\frac{t}{t_0}\bigg)z^{2/3}\bigg\} \\ &- Bi(-z^{2/3})Ai\bigg\{-\bigg(1-\frac{t}{t_0}\bigg)z^{2/3}\bigg\}\bigg]^2, \end{aligned} \tag{D2}$$

where Ai and Bi are Airy functions and Ai' and Bi' denotes their derivatives respectively.

In the quench limit, $\omega_P t_0 \ll 1$, the Airy functions can be expanded in power series of z of the form

$$\begin{aligned} Ai(z) &\approx \frac{1}{3^{2/3}\Gamma\left(\frac{2}{3}\right)}\left(1+\frac{z^3}{6}\right) - \frac{z}{3^{1/3}\Gamma\left(\frac{1}{3}\right)}, \\ Bi(z) &\approx \frac{1}{3^{1/6}\Gamma\left(\frac{2}{3}\right)}\left(1+\frac{z^3}{6}\right) - \frac{z3^{1/6}}{\Gamma\left(\frac{1}{3}\right)}, \\ Ai'(z) &\approx \frac{1}{3^{1/3}\Gamma\left(\frac{1}{3}\right)}\left(1+\frac{z^3}{3}\right) - \frac{z^2}{2\times 3^{2/3}\Gamma\left(\frac{2}{3}\right)}, \\ Bi'(z) &\approx \frac{3^{1/6}}{\Gamma\left(\frac{1}{3}\right)}\left(1+\frac{z^3}{3}\right) - \frac{z^2}{2\times 3^{1/6}\Gamma\left(\frac{2}{3}\right)}, \end{aligned} \tag{D3}$$

Collecting the coefficients of the leading powers of z, we obtain Eq. (77) as

$$\Sigma(t) = \frac{3\alpha}{2\omega_P}\left(1+\frac{t^3\omega_P^2}{3t_0}\right), \quad \omega_P \ll 1/t_0. \tag{D4}$$

On the other hand, in the adiabatic limit $\omega_P t_0 \gg 1$, we get the same answer as the time-independent harmonic oscillator with its mass term ω_P^2 replaced by $\omega_P^2 + m(t)$.

[1] D. Basov, R. Averitt, and D. Hsieh, Nat. Mater. **16**, 1077 (2017).

[2] M. Buzzi, M. Först, R. Mankowsky, and A. Cavalleri, Nat. Rev. Mater. **3**, 299 (2018).

[3] J. Bloch, A. Cavalleri, V. Galitskii, M. Harezi, and A. Rubio, Nature (London) **606**, 41 (2022).

[4] M. C. Hoffmann and J. A. Fülöp, J. Phys. D **44**, 083001 (2011).

[5] T. Kampfrath, K. Tanaka, and K. A. Nelson, Nat. Photon. **7**, 680 (2013).

[6] D. Nicoletti and A. Cavalleri, Adv. Opt. Photon. **8**, 401 (2016).

[7] M. Rini, R. Tobey, N. Dean, J. Itatani, Y. Tomioka, Y. Tokura, R. W. Schoenlein, and A. Cavalleri, Nature (London) **449**, 72 (2007).

[8] R. Mankowsky, M. Först, and A. Cavalleri, Rep. Prog. Phys. **79**, 064503 (2016).

[9] M. Först, C. Manzoni, S. Kaiser, Y. Tomioka, Y.-N. Tokura, R. Merlin, and A. Cavalleri, Nat. Phys. **7**, 854 (2011).

[10] X. Li, T. Qiu, J. Zhang, E. Baldini, J. Lu, A. M. Rappe, and K. A. Nelson, Science **364**, 1079 (2019).

[11] T. F. Nova, A. S. Disa, M. Fechner, and A. Cavalleri, Science **364**, 1075 (2019).

[12] A. Disa, T. Nova, and A. Cavalleri, Nat. Phys. **17**, 1087 (2021).

[13] E. Abreu, Nat. Phys. **18**, 375 (2022).

[14] M. Henstridge, M. Först, E. Rowe, M. Fechner, and A. Cavalleri, Nat. Phys. **18**, 457 (2022).

[15] M. Porer, M. Fechner, E. M. Bothschafter, L. Rettig, M. Savoini, V. Esposito, J. Rittmann, M. Kubli, M. J. Neugebauer, E. Abreu, T. Kubacka, T. Huber, G. Lantz, S. Parchenko, S. Grübel, A. Paarmann, J. Noack, P. Beaud, G. Ingold, U. Aschauer, S. L. Johnson, and U. Staub, Phys. Rev. Lett. **121**, 055701 (2018).

[16] H. Zhang *et al.*, Nat. Phys. **19**, 545 (2023).

[17] J. Zhang and R. Averitt, Annu. Rev. Mater. Res. **44**, 19 (2014).

[18] A. de la Torre, D. M. Kennes, M. Claassen, S. Gerber, J. W. McIver, and M. A. Sentef, Rev. Mod. Phys. **93**, 041002 (2021).

[19] C. Bao, P. Tang, D. Sun, and S. Zhou, Nat. Rev. Phys. **4**, 33 (2022).

[20] A. Subedi, A. Cavalleri, and A. Georges, Phys. Rev. B **89**, 220301(R) (2014).

[21] A. Subedi, Phys. Rev. B **95**, 134113 (2017).

[22] A. P. Itin and M. I. Katsnelson, Phys. Rev. B **97**, 184304 (2018).

[23] K. A. Müller and H. Burkard, Phys. Rev. B **19**, 3593 (1979).

[24] J. G. Bednorz and K. A. Müller, Phys. Rev. Lett. **52**, 2289 (1984).

[25] M. Itoh, R. Wang, Y. Inaguma, T. Yamaguchi, Y.-J. Shan, and T. Nakamura, Phys. Rev. Lett. **82**, 3540 (1999).

[26] J. Haeni, P. Irvin, W. Chang, R. Uecker, P. Reiche, Y. Li, S. Choudhury, W. Tian, M. Hawley, B. Craigo *et al.*, Nature (London) **430**, 758 (2004).

[27] O. Kvyatkovskii, Phys. Solid State **43**, 1401 (2001).

[28] S. Rowley, L. Spalek, R. Smith, M. Dean, M. Itoh, J. Scott, G. Lonzarich, and S. Saxena, Nat. Phys. **10**, 367 (2014).

[29] P. Chandra, G. Lonzarich, S. Rowley, and J. Scott, Rep. Prog. Phys. **80**, 112502 (2017).

[30] S. M. Griffin, M. Lilienblum, K. T. Delaney, Y. Kumagai, M. Fiebig, and N. A. Spaldin, Phys. Rev. X **2**, 041022 (2012).

[31] S. Ulm, J. Roßnagel, G. Jacob, C. Degünther, S. Dawkins, U. Poschinger, R. Nigmatullin, A. Retzker, M. Plenio, F. Schmidt-Kaler *et al.*, Nat. Commun. **4**, 2290 (2013).

[32] S.-Z. Lin, X. Wang, Y. Kamiya, G.-W. Chern, F. Fan, D. Fan, B. Casas, Y. Liu, V. Kiryukhin, W. H. Zurek *et al.*, Nat. Phys. **10**, 970 (2014).

[33] P. Gagel, P. P. Orth, and J. Schmalian, Phys. Rev. Lett. **113**, 220401 (2014).

[34] P. Gagel, P. P. Orth, and J. Schmalian, Phys. Rev. B **92**, 115121 (2015).

[35] A. Chiocchetta, M. Tavora, A. Gambassi, and A. Mitra, Phys. Rev. B **91**, 220302(R) (2015).

[36] P. Jurcevic, H. Shen, P. Hauke, C. Maier, T. Brydges, C. Hempel, B. P. Lanyon, M. Heyl, R. Blatt, and C. F. Roos, Phys. Rev. Lett. **119**, 080501 (2017).

[37] M. Heyl, Rep. Prog. Phys. **81**, 054001 (2018).

[38] M. Heyl, Europhys. Lett. **125**, 26001 (2019).

[39] M. Knap, M. Babadi, G. Refael, I. Martin, and E. Demler, Phys. Rev. B **94**, 214504 (2016).

[40] D. Kennes, E. Wilner, D. Weichman, and A. Millis, Nat. Phys. **13**, 479 (2017).

[41] D. Shin, S. Sato, H. H., U. De Giovanni, N. Park, and A. Rubio, NPJ Comp. Mater. **6**, 182 (2020).

[42] M.-X. Guan, E. Wang, P. You, J. Sun, and S. Meng, Nat. Commun. **12**, 185 (2021).

[43] F. Grandi, J. Li, and M. Eckstein, Phys. Rev. B **103**, L041110 (2021).

[44] A. Klein, M. H. Christensen, and R. M. Fernandes, Phys. Rev. Res. **2**, 013336 (2020).

[45] M. Puviani and M. A. Sentef, Phys. Rev. B **98**, 165138 (2018).

[46] D. Shin, S. Latini, C. Schafer, S. A. Sato, E. Baldini, U. De Giovannini, H. Hubener, and A. Rubio, Phys. Rev. Lett. **129**, 167401 (2022).

[47] D. Shin, S. Latini, C. Schäfer, S. A. Sato, U. De Giovannini, H. Hübener, and A. Rubio, Phys. Rev. B **104**, L060103 (2021).

[48] D. Kuzmanovski, G. Aeppli, H. M. Rønnow, and A. V. Balatsky, Kapitza stabilization of a quantum critical order (2022).

[49] A. Ashkin, Phys. Rev. Lett. **24**, 156 (1970).

[50] A. Ashkin, Science **210**, 1081 (1980).

[51] C. Bustamante, Y. Chemla, S. Liu, and M. D. Wang, Nat. Rev. Meth. Prim. **1**, 25 (2021).

[52] G. Duffing, *Erzwungene Schwingungen bei veränderlicher Eigenfrequenz and ihretechnische Bedaeutung* (F. Vieweg & Sohn, Braunschweig, 1918).

[53] S. H. Strogatz, *Nonlinear Dynamics and Chaos: With Applications to Physics, Biology, Chemistry, and Engineering* (CRC Press, 2018).

[54] A. K. Chatterjee, A. Kundu, and M. Kulkarni, Phys. Rev. E **102**, 052103 (2020).

[55] R. W. Boyd, *Nonlinear Optics* (Academic Press, 2020).

[56] A. J. Lichtenberg and M. A. Lieberman, *Regular and Stochastic Motion* (Springer, Berlin, 1983).

[57] A. Kamenev, *Field Theory of Non-Equilibrium Systems* (Cambridge University Press, 2011).

[58] J. Schwinger, Proc. Natl. Acad. Sci. USA **37**, 452 (1951).

[59] A. Altland and B. D. Simons, *Condensed Matter Field Theory* (Cambridge University Press, 2010).